

1 **Energy-conservation datasets of global land surface radiation**
2 **and heat fluxes from 2000-2020 generated by CoSEB**

3 Junrui Wang^{a, b}, Ronglin Tang^{a, b, *}, Meng Liu^c, Zhao-Liang Li^{a, b, c}

4 ^a State Key Laboratory of Resources and Environment Information System, Institute of
5 Geographic Sciences and Natural Resources Research, Chinese Academy of Sciences,
6 Beijing 100101, China

7 ^b University of Chinese Academy of Sciences, Beijing 100049, China

8 ^c State Key Laboratory of Efficient Utilization of Arable Land in China, Institute of
9 Agricultural Resources and Regional Planning, Chinese Academy of Agricultural
10 Sciences, Beijing 100081, China

11 * Authors to whom correspondence should be addressed: tangrl@lreis.ac.cn

12 **Abstract**

13 Accurately estimating global land surface radiation [including downward
14 shortwave radiation (SW_{IN}), downward longwave radiation (LW_{IN}), upward shortwave
15 radiation (SW_{OUT}), upward longwave radiation (LW_{OUT}) and net radiation (Rn)] and heat
16 fluxes [including latent heat flux (LE), soil heat flux (G) and sensible heat flux (H)] is
17 essential for quantifying the exchange of radiation, heat and water between the land and
18 atmosphere under global climate change. This study presents the first data-driven
19 energy-conservation datasets of global land surface radiation and heat fluxes from 2000
20 to 2020, generated by our model of Coordinated estimates of land Surface Energy
21 Balance components (CoSEB). The model integrates GLASS and MODIS remote
22 sensing data, ERA5-Land reanalysis datasets, topographic data, CO₂ concentration data
23 as independent variables and in situ radiation and heat flux observations at 258 eddy
24 covariance sites worldwide as dependent variables within a multivariate random forest
25 technique to effectively learn the physics of energy conservation. The developed
26 CoSEB-based datasets are strikingly advantageous in that [1] they are the first data-
27 driven global datasets that satisfy both surface radiation balance and heat balance

28 among the eight fluxes, as demonstrated by both the radiation imbalance ratio [RIR, 29 defined as $100\% \times (SW_{IN} - SW_{OUT} + LW_{IN} - LW_{OUT})/Rn$] and energy imbalance ratio 30 [EIR, defined as $100\% \times (Rn - G - LE - H)/Rn$] of 0, [2] the radiation and heat fluxes 31 are characterized by high accuracies, where (1) the RMSEs (R^2) for daily estimates of 32 SW_{IN} , SW_{OUT} , LW_{IN} , LW_{OUT} , Rn , LE , H and G from the CoSEB-based datasets at 44 independent test sites were 37.52 W/m^2 (0.81), 14.20 W/m^2 (0.42), 22.47 W/m^2 (0.90), 33 13.78 W/m^2 (0.95), 29.66 W/m^2 (0.77), 30.87 W/m^2 (0.60), 29.75 W/m^2 (0.44) and 5.69 W/m^2 (0.44), respectively, (2) the CoSEB-based datasets, in comparison to the 35 mainstream products/datasets (i.e. GLASS, BESS-Rad, BESSV2.0, FLUXCOM, 36 MOD16A2, PML_V2 and ETMonitor) that generally separately estimated subsets of 37 the eight flux components, better agreed with the in situ observations. Our developed 38 datasets hold significant potential for application across diverse fields such as 39 agriculture, forestry, hydrology, meteorology, ecology, and environmental science, 40 which can facilitate comprehensive studies on the variability, impacts, responses, 41 adaptation strategies, and mitigation measures of global and regional land surface 42 radiation and heat fluxes under the influences of climate change and human activities. 43 The CoSEB-based datasets are open access and available through the National Tibetan 44 Plateau Data Center (TPDC) at <https://doi.org/10.11888/Terre.tpdc.302559> (Tang et al., 45 2025a) and through the Science Data Bank (ScienceDB) at 46 <https://doi.org/10.57760/sciencedb.27228> (Tang et al., 2025b).

47 **Key words:** Surface energy balance; Surface radiation balance; Shortwave/Longwave
48 radiation; Net radiation; Sensible/Latent heat flux; Evapotranspiration; CoSEB

50 **1 Introduction**

51 Land surface radiation balance and heat balance play important roles in Earth's 52 climate system, representing the physical processes by which the surface-atmosphere 53 absorbs and redistributes radiation and heat fluxes (Berbery et al., 1999; Betts et al., 54 1996; Mueller et al., 2009; Sellers et al., 1997; Xu et al., 2022a), and facilitating the 55 exchange of water, energy, carbon, and other agents essential to climatic and ecological

systems and human society (Jia et al., 2013; Wang et al., 2012; Wild, 2009; Wild et al., 2012; Xia et al., 2006). Accurately monitoring the spatial and temporal variations of global land surface radiation [including downward shortwave radiation (SW_{IN}), downward longwave radiation (LW_{IN}), upward shortwave radiation (SW_{OUT}), upward longwave radiation (LW_{OUT}) and net radiation (Rn)] and heat fluxes [including latent heat flux (LE), soil heat flux (G) and sensible heat flux (H)] is indispensable for quantifying the exchange of radiation, heat and water between the land and atmosphere under global climate change (Ersi et al., 2024; Liang et al., 2019; Rios & Ramamurthy, 2022; Tang et al., 2024a; Wang et al., 2021), and for studying solar energy utilization (Tang et al., 2024b; Zhang et al., 2017), hydrological cycle (Huang et al., 2015; Wild & Liepert, 2010), ecosystem productivity (Nemani et al., 2003), agricultural management (De Wit et al., 2005) and ecological protection (Tang et al., 2023). Remote sensing (RS) technology, with its high spatial-temporal resolution and applicability over large areas, is considered to be the most effective and economical means for obtaining global land surface radiation and heat fluxes (Liu et al., 2016; Van Der Tol, 2012; Zhang et al., 2010).

In past decades, numerous RS-based products/datasets of global surface radiation and heat fluxes have significantly advanced, which were generally generated by physical (Li et al., 2023; Mu et al., 2011; Yu et al., 2022) or statistical methods (Jiao et al., 2023; Jung et al., 2019; Peng et al., 2020). However, two key limitations still exist in these products. Firstly, most available products provide only a single component of land surface radiation or heat fluxes, e.g. ETMonitor (Zheng et al., 2022) and MOD16A2 (Mu et al., 2011) only estimating LE, leading to the failure to satisfy surface radiation balance and heat balance when the single radiation or heat flux is utilized in conjunction with products containing other radiation and heat components (Wang et al., 2025), and further posing significant uncertainties to understand the interactions and redistributions of surface radiation and energy in the Earth-atmosphere system. Secondly, a few products, e.g., FLUXCOM (Jung et al., 2019) and GLASS (Jiang et al.,

84 2015; Zhang et al., 2014), generated datasets for multiple components of surface
85 radiation and heat fluxes by using separate estimates from the uncoordinated models,
86 which make them difficult to abide by surface radiation and heat conservation. These
87 energy-imbalanced and radiation-imbalanced estimates among multiple components
88 from previous products/datasets severely limit their in-depth applications in analyzing
89 the spatial and temporal trends, simulating the physical processes of radiation, heat and
90 water cycles as well as revealing the attributions and mechanisms in Earth-surface
91 system under global climate change. It was imperative to develop global datasets of
92 land surface radiation and heat fluxes characterized by high ~~accuraciesaccuracy~~,
93 radiation balance as well as heat balance, to better meet the requirements in practical
94 applications of various fields.

95 Our proposed data-driven model/framework of Coordinated estimates of land
96 Surface Energy Balance components (CoSEB) (Wang et al., 2025), which effectively
97 learns the underlying physical interrelations (i.e., surface energy conservation law)
98 among multiple targeted variables, provides an unprecedented opportunity to develop
99 global datasets of land surface radiation and heat fluxes that can not only
100 simultaneously provide high-accuracy estimates of these components but also adhere
101 to surface radiation- and heat-conservation laws.

102 The objectives of this study are twofold: (1) to develop high-accuracy datasets of
103 global land surface radiation and heat fluxes, which comply with the principles of
104 radiation balance and heat balance, using our CoSEB model renewed based on in situ
105 observations, remote sensing data and reanalysis datasets; (2) to validate the
106 datasets/model estimates against data from in situ observations, mainstream products
107 as well as estimates from uncoordinated random forest (RF) techniques. Section 2
108 introduces the data resources used in this study. Section 3 briefly describes the method
109 we used to estimate global surface radiation and heat fluxes. Section 4 presents the
110 evaluation of the datasets/model estimates generated by our renewed CoSEB model.
111 Section 5 discusses the superiority, potential applications and uncertainties of the

112 developed datasets. Data availability is given in Section 6, and a summary and
113 conclusion is provided in Section 7.

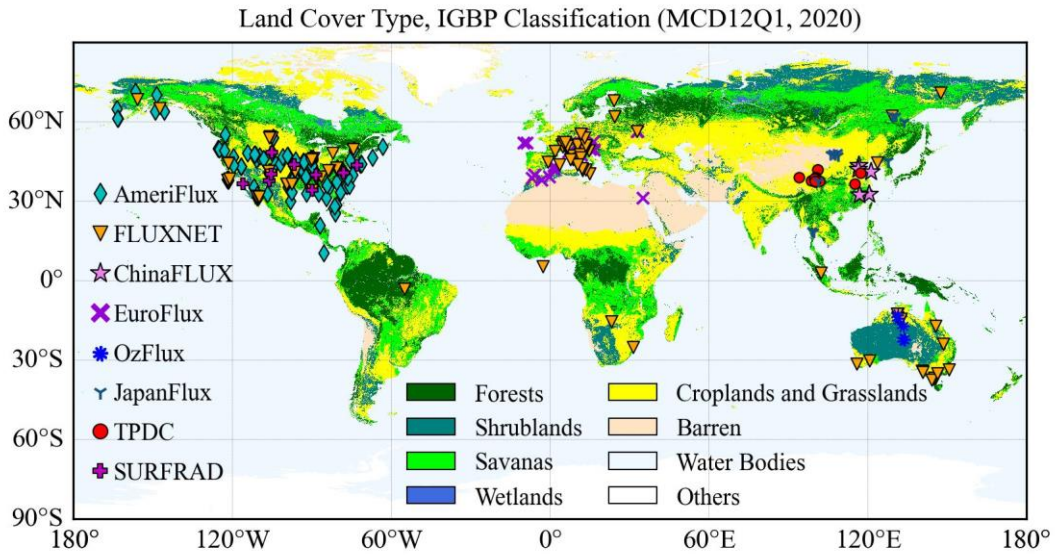
114 **2 Data**

115 **2.1 Ground-based observations**

116 In this study, the in situ observations of land surface radiation and heat fluxes at
117 302 eddy covariance (EC) sites from the networks of AmeriFlux (174 sites, 2000–2020,
118 <https://AmeriFlux.lbl.gov/Data/>, last access: 6 August 2024), EuroFlux (72 sites, 2000-
119 2020, <http://www.europe-fluxdata.eu/>, last access: 6 August 2024), OzFlux (5 sites,
120 2007-2012, <https://data.ozflux.org.au/>, last access: 6 August 2024), FLUXNET (108
121 sites, 2000–2014, <https://FLUXNET.org/Data/download-Data/>, last access: 6 August
122 2024), JapanFlux (15 sites, 2001-2020, <https://ads.nipr.ac.jp/japan-flux2024/>, last
123 access: 10 October 2025), ChinaFLUX (5 sites, 2005-2020, <http://www.chinaflux.org/>,
124 last access: 6 August 2024) and National Tibetan Plateau/Third Pole Environment Data
125 Center (TPDC, 13 sites, 2012–2020, <https://Data.tpdc.ac.cn/en/Data>, last access: 6
126 August 2024) were used (Fig. 1), where 37, 48 and 5 sites in FLUXNET were also
127 shared in AmeriFlux, EuroFlux and OzFlux, respectively. These 302 sites were filtered
128 out from all collected 1098 sites by following the quality-assurance and quality-control
129 steps, including: (1) any site with a missing component of any of the SW_{IN} , SW_{OUT} , LW_{IN} ,
130 LW_{OUT} , LE, H and G was excluded, reducing the 1098 sites to 472 sites for further
131 analysis; (2) any half-hour period with missing data for any of these components was
132 excluded; (3) the half-hourly ground-based observations with quality-control flag of 2
133 or 3 (bad quality) were removed but quality-control flag of 0 and 1 (good quality) were
134 maintained; (4) a daily average of the half-hour observations was calculated for each
135 day with greater than 80% good-quality data, further reducing the 472 sites to 355 sites;
136 (5) the aggregated daily LE and H were corrected for energy imbalance using the
137 Bowen ratio method when the daily energy balance closure [defined as
138 $(LE + H) / (Rn - G)$] varied between 0.2 and 1.8 following Wang et al. (2025) to

139 exclude physically implausible measurements; (6) extreme outliers in the daily
140 evaporative fraction were further removed by excluding values outside the 1st–99th
141 percentile range, a common practice in flux and remote sensing studies (Bartkowiak et
142 al., 2024; Wang et al., 2023), further reducing the 355 sites to 337 sites. Besides, the RS
143 products/datasets involved in this study collocated at the sites should not be missing,
144 finally reducing the 337 sites to 302 sites for analysis. Note that the Rn at these sites
145 used in this study was calculated from the sum of net longwave radiation (LW_{IN} minus
146 LW_{OUT}) and net shortwave radiation (SW_{IN} minus SW_{OUT}), rather than using the
147 observed Rn directly, to ensure surface radiation balance in training datasets.

148 These 302 sites used in this study cover a wide range of global climate regimes
149 across 14 land cover types, including (1) evergreen needleleaf forests (ENF, 55 sites);
150 (2) evergreen broadleaf forests (EBF, 12 sites); (3) deciduous needleleaf forests (DNF,
151 7 sites); (4) deciduous broadleaf forests (DBF, 40 sites); (5) mixed forests (MF, 8 sites);
152 (6) closed shrublands (CSH, 5 sites); (7) open shrublands (OSH, 11 sites); (8) woody
153 savannas (WSA, 6 sites); (9) savannas (SAV, 10 sites); (10) grasslands (GRA, 62 sites);
154 (11) permanent wetlands (WET, 22 sites); (12) croplands (CRO, 59 sites); (13) water
155 bodies (WAT, 1 sites); (14) cropland/natural vegetation mosaics (CVM, 4 sites). Among
156 them, 44 sites (~15% of the total, see Table S1) were isolated to serve as spatially
157 independent sites to test the generated datasets and they did not participate in the
158 development of the model/datasets.



159

160 **Fig. 1 Spatial distribution of the 302 eddy covariance sites from AmeriFlux, FLUXNET,**
 161 **EuroFlux, OzFlux, JapanFlux, ChinaFLUX and TPDC, and nine radiation sites from**
 162 **SURFRAD involved for analysis in this study.**

163

164 Furthermore, ground-based radiation observations from nine sites that are located
 165 in large flat agricultural areas covered by crops and grasses from SURFRAD
 166 (<https://gml.noaa.gov/>) were also introduced to validate land surface radiation estimates.
 167 Similar to the preprocessing performed on the observations of the 302 EC sites, the
 168 SW_{IN} , SW_{OUT} , LW_{IN} , LW_{OUT} and Rn from the SURFRAD were also quality-controlled
 169 and aggregated to daily data. Spatial distribution of the 302 EC sites and nine radiation
 170 sites from SURFRAD are shown in Fig. 1, with site details (latitude, longitude, land
 171 cover types, digital elevation model and temporal coverage) provided in Supplementary
 Tables S1 and S2.

172

2.2 Climate/meteorology and remote sensing data

173

174 To generate global datasets of land surface radiation and heat fluxes from 2000 to
 175 including:

176 (1) ERA5-Land reanalysis datasets (<https://cds.climate.copernicus.eu/>, last access: 6

177 August 2024) with the spatial resolution of ~9 km from 1950 (Muñoz-Sabater et
 178 al., 2021). Following our previous work (Wang et al., 2025), this study used

179 variables from the ERA5-Land datasets to drive the model, including near-surface
180 2 m air temperature (T_a), soil temperature in layer 1 (0-7 cm, T_{S1}), soil volumetric
181 moisture content in layer 1 (0-7 cm, SMI), solar radiation reaching the surface of
182 the earth (SW_{IN}^{ERA5}), net thermal radiation at the surface (LW_{net}), pressure of the
183 atmosphere (PA), 10 m wind speed (WS), precipitation (P_r) and the 2 m dewpoint
184 temperature, daily minimum and maximum air temperature [for calculating
185 relative air humidity (RH)].

186 (2) GLASS datasets (<https://glass.bnu.edu.cn/>, last access: 6 August 2024), which
187 provide the 500 m 8-day leaf area index (LAI) and fractional vegetation cover
188 (FVC) from February 2000 to December 2021.

189 (3) MOD44B product (<https://lpdaac.usgs.gov/>, last access: 6 August 2024), which
190 offers yearly 250 m percent tree cover (PTC) since 2000, representing the
191 percentage (0~100%) of a pixel covered by tree canopy.

192 (4) NOAA/GML atmospheric carbon dioxide (CO_2) concentration data, providing
193 monthly global marine surface mean data since 1958
194 (ftp://aftp.cmdl.noaa.gov/products/trends/co2/co2_mm_gl.txt, last access: 6
195 August 2024).

196 (5) GMTED2010 topographic data
197 (https://topotools.cr.usgs.gov/gmted_viewer/gmted2010_global_grids.php, last
198 access: 6 August 2024), providing 500 m digital elevation model (DEM), slope,
199 and aspect.

200 The ~9 km ERA5-Land datasets were spatially interpolated to 500 m using the
201 cubic convolution method, and the 250 m PTC was resampled to 500 m using the
202 arithmetic averaging method.

203 2.3 Mainstream datasets/products for inter-comparison

204 Mainstream RS-based datasets/products of moderate-resolution global land
205 surface radiation and heat fluxes were collected for inter-comparison (Table 1),

206 including (1) the daily 0.05° GLASS SW_{IN} , LW_{IN} , LW_{OUT} and Rn products from 2000 to
207 2018 (<https://glass.bnu.edu.cn/>, last access: 6 August 2024), (2) the daily 0.05°
208 Breathing Earth System Simulator Radiation (BESS-Rad) SW_{IN} products from 2000 to
209 2020 (<https://www.environment.snu.ac.kr/bess-rad>), (3) the daily 0.05° BESS
210 Version2.0 (BESSV2.0) Rn and LE products from 2000 to 2020
211 (<https://www.environment.snu.ac.kr/bessv2>), (4) the 8-day 0.0833° FLUXCOM Rn, LE
212 and H products from 2001 to 2020 (<https://fluxcom.org/>, last access: 6 August 2024),
213 (5) the daily 1 km ETMonitor LE product from 2000 to 2020 (<https://data.casearth.cn/>,
214 last access: 6 August 2024), (6) the 8-day 500 m Penman-Monteith-Leuning Version2
215 (PML_V2, <https://www.tpdc.ac.cn/>, last access: 6 August 2024) LE product from 2000
216 to 2020; and (7) the 8-day 500 m MOD16A2 (<https://lpdaac.usgs.gov/>, last access: 6
217 August 2024) LE product from 2000 to 2020.

218 The GLASS SW_{IN} products are derived from a combination of the GLASS
219 broadband albedo product and the surface shortwave net radiation estimates, where the
220 surface shortwave net radiation is estimated using linear regression with MODIS top-
221 of-atmosphere (TOA) spectral reflectance (Wang et al., 2015). The GLASS LW_{IN} and
222 LW_{OUT} products are generated using densely connected convolutional neural networks,
223 incorporating Advanced Very High-Resolution Radiometer (AVHRR) TOA reflectance
224 and ERA5 near-surface meteorological data (Xu et al., 2022b). The GLASS Rn
225 products are estimated from the meteorological variables from MERRA2 and surface
226 variables from GLASS using the multivariate adaptive regression splines model (Jiang
227 et al., 2015). The BESS-Rad and BESSV2.0 estimate SW_{IN} and Rn using a radiative
228 transfer model (i.e., Forest Light Environmental Simulator, FLiES) with an artificial
229 neural network based on MODIS and MERRA2 reanalysis datasets, and using FLiES
230 based on MODIS products and NCEP/NCAR reanalysis data, respectively (Li et al.,
231 2023; Ryu et al., 2018). Moreover, the BESSV2.0 (Li et al., 2023), MOD16A2 (Mu et
232 al., 2011), PML_V2 (Zhang et al., 2019) and ETMonitor (Zheng et al., 2022) generated
233 global LE by physical models, such as Penman-Monteith equation, Priestley-Taylor

234 equation and/or Shuttleworth-Wallace two-source scheme. The FLUXCOM Rn, LE and
 235 H datasets are obtained through multiple machine learning methods based on in situ
 236 observations from FLUXNET and remote sensing and meteorological data (Jung et al.,
 237 2019). For better consistency, RF-based 8-day 0.0833° Rn and Bowen ratio-corrected
 238 LE and H for the periods of 2000 to 2020 from the FLUXCOM were used in this study.

239 **Table 1 Summary of mainstream datasets/products for inter-comparison used in this study**

| Products/ datasets | Reso- lution | Time coverage | Variables | Algorithms | References |
|-----------------------|-------------------|------------------|---|--|--|
| GLASS | 0.05°/ daily | 2000- 2018 | SW_{IN} , LW_{IN} , LW_{OUT} , Rn | Machine learning, direct estimation algorithm | Wang et al. (2015); Xu et al. (2022b); Jiang et al. (2015) |
| BESS-Rad | 0.05°/ daily | 2000- 2020 | SW_{IN} | BESS process model | Ryu et al. (2018) |
| BESSV2.0 | 0.05°/ daily | 2000- 2020 | Rn, LE | BESS process model | Li et al. (2023) |
| FLUXCOM | 0.0833°/ 8-day | 2000- 2020 | Rn, LE, H | Model tree ensembles | Jung et al. (2019) |
| MOD16A2 | 500 m/ 8-day | 2000- 2020 | LE | Modified Penman- Monteith equation Penman Monteith- Leuning model, <u>Priestley</u> <u>Priestly</u> Taylor equation and Gash model | Mu et al. (2011) |
| PML_V2 | 500 m/ 8-day | 2002- 2020 | LE | Shuttleworth- Wallace two- source scheme, Gash model and Penman equation | Zhang et al. (2019) |
| ETMonitor | 1 km/ daily | 2000- 2020 | LE | Gash model and Penman equation | Zheng et al. (2022) |

240 **3 Methods**

241 The method used to generate global datasets of land surface radiation and heat
 242 fluxes is based on the CoSEB model/framework, which was developed by our
 243 previously published work (Wang et al., 2025), to coordinately estimate global land
 244 surface energy balance components (including Rn, LE, H and G) using the multivariate

245 random forest technique, with a combination of MODIS and GLASS products, ERA5-
246 Land reanalysis datasets, and in situ observations at 336 EC sites. The CoSEB model
247 was demonstrated to be able to produce high-accuracy estimates of land surface energy
248 components, with the RMSE of $<17 \text{ W/m}^2$ and R^2 of > 0.83 for estimating 4-day Rn,
249 LE and H, and the RMSE of $<5 \text{ W/m}^2$ and R^2 of 0.55 for estimating 4-day G. The most
250 praiseworthy superiority of the CoSEB model lies in its ability to balance the land
251 surface energy components, with an energy imbalance ratio [EIR, defined as $100\% \times$
252 $(Rn - G - LE - H)/Rn$] of 0.

253 To coordinately estimate land surface radiation and heat fluxes that comply with
254 both radiation balance and heat balance, one of the key procedures in the construction
255 of the CoSEB model was to prepare training datasets that satisfy surface radiation and
256 heat balance. For this purpose, the energy-imbalance corrections on daily in situ
257 observed LE and H were conducted by the most widely applied Bowen ratio method
258 $[H^{corr} = \frac{H}{H+LE} \times (Rn - G), LE^{corr} = \frac{LE}{H+LE} \times (Rn - G)]$, where H^{corr} and LE^{corr}
259 represent the sensible heat flux and latent heat flux after energy-imbalance correction,
260 respectively] with the aid of Rn and G observations, and the in situ Rn was calculated
261 from the sum of in situ observed net longwave radiation (LW_{IN} minus LW_{OUT}) and net
262 shortwave radiation (SW_{IN} minus SW_{OUT}). The input variables to renew the CoSEB
263 model include: (1) climate/meteorology: T_a , SW_{IN}^{ERA5} , LW_{net} , WS , PA , P_r , RH ,
264 CO_2 concentration; (2) vegetation and soil: LAI , FVC , PTC , T_{SI} , SMI ; (3) topography
265 data: DEM , *Slope* and *Aspect*, in addition to longitude (*Lon*), latitude (*Lat*), and inverse
266 relative distance from the Earth to the Sun (dr), in which the dr was calculated as

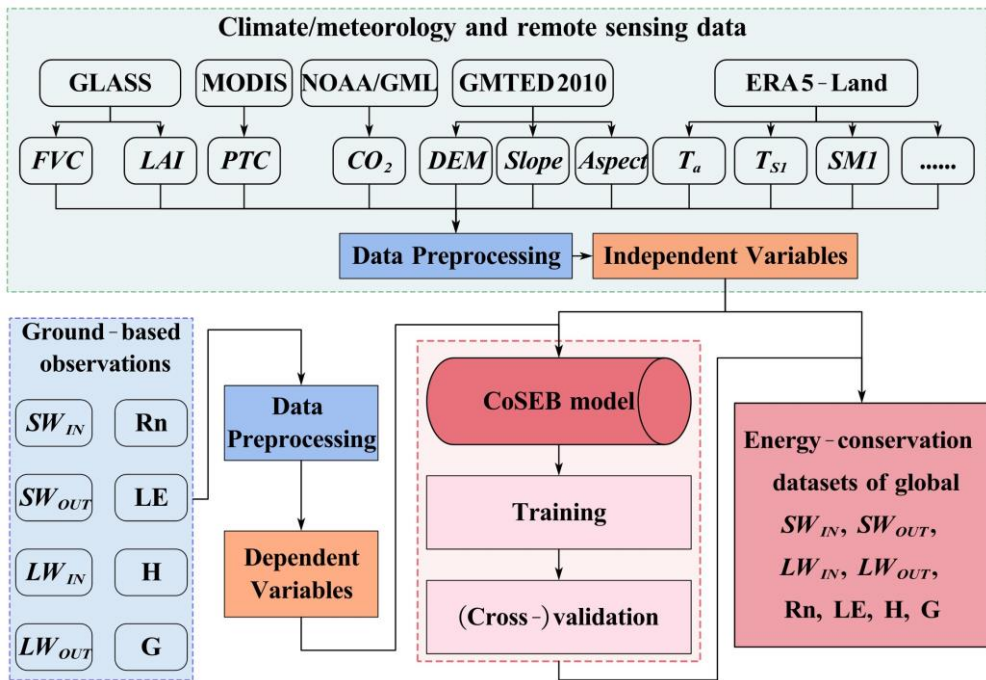
$$267 dr = 1 + 0.033 \times \cos\left(\frac{2\pi \times DOY}{365}\right), \text{ where } DOY \text{ represents the day of year. Considering}$$

268 that the footprint of the site-based measurements of turbulent heat fluxes is generally at
269 a scale of hundreds of meters, to reduce the effect of differences of spatial scales
270 between ground-based measurements (dependent variables) and remotely
271 sensed/reanalysis datasets (independent variables), we renewed the CoSEB model at a

272 spatial scale of 500 m for coordinately estimating global daily land surface radiation
273 and heat fluxes, which can be expressed as follows:

274
$$\begin{pmatrix} SW_{IN}, SW_{OUT}, LW_{IN}, \\ LW_{OUT}, Rn, LE, H, G \end{pmatrix} = f \begin{pmatrix} Lon, Lat, T_a, T_{S1}, SM1, SW_{IN}^{ER45}, LW_{net}, PA, WS, P_r, dr \\ RH, LAI, FVC, PTC, DEM, Slope, Aspect, CO_2 \end{pmatrix} \quad (1)$$

275 To enhance model generalization, the renewed CoSEB model was reoptimized
276 using random and grid search methods, resulting in different hyperparameters of 281
277 decision trees, a maximum depth of 21, and minimum samples split and leaf of 8 from
278 those of Wang et al. (2025). Site-based 10-fold cross-validation was employed to
279 evaluate the transferability and generalization of the CoSEB model by randomly
280 dividing all sites into ten folds, where the samples from each fold of sites in turn served
281 as validation datasets while the remaining folds were used as training datasets, ensuring
282 that the validation was conducted on sites spatially independent from the training data.
283 Furthermore, to benchmark the coordinated estimates from the renewed CoSEB model,
284 eight RF-based uncoordinated models were constructed, each separately estimating one
285 of SW_{IN} , SW_{OUT} , LW_{IN} , LW_{OUT} , Rn , LE , H or G using the same inputs as those in the
286 renewed CoSEB model. Fig. 2 illustrates the flowchart for generating global datasets
287 of land surface radiation and heat fluxes by the CoSEB model.



288

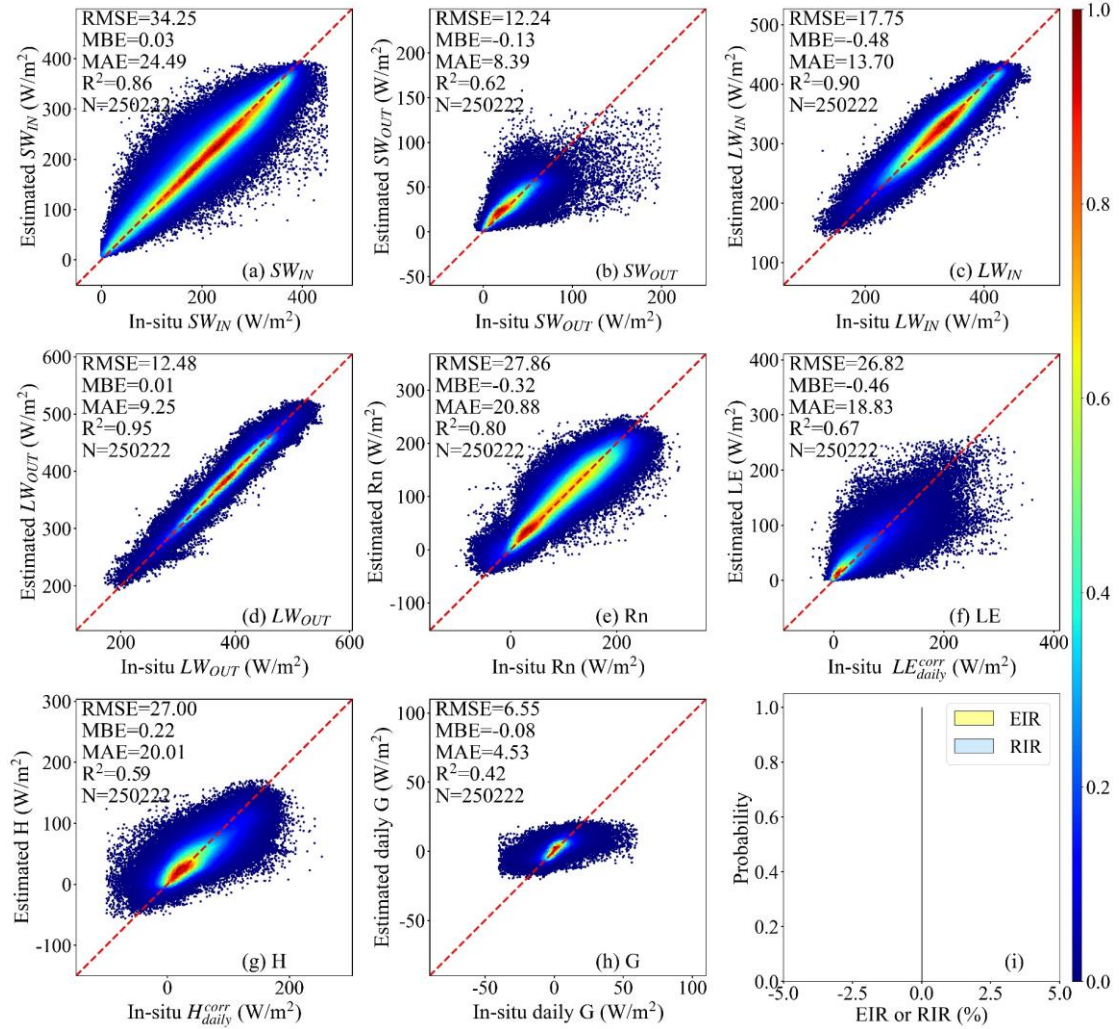
289 **Fig. 2 Flowchart for generating energy-conservation datasets of global land surface radiation**
290 [including downward shortwave radiation (SW_{IN}), downward longwave radiation (LW_{IN}),
291 upward shortwave radiation (SW_{OUT}), upward longwave radiation (LW_{OUT}) and net radiation
292 (Rn) and heat fluxes [including latent heat flux (LE), soil heat flux (G) and sensible heat flux
293 (H)] by the CoSEB model renewed from in situ observations at 258 sites worldwide and
294 collocated remote sensing and reanalysis datasets.

295 **4 Results**296 **4.1 Validation of the CoSEB model**297 **4.1.1 Site-based 10-fold cross-validations at 258 EC sites**

298 Fig. 3 and Fig. 4 present the scatter density plots of the site-based 10-fold cross-
299 validation of daily SW_{IN} , LW_{IN} , SW_{OUT} , LW_{OUT} , Rn , LE , H and G estimated from the
300 renewed CoSEB model and the RF-based uncoordinated models, respectively, by using
301 the validation datasets collected at 258 EC sites worldwide. Results indicated that the
302 estimates from both the CoSEB model and the RF-based uncoordinated models agreed
303 well with the in situ observations, with the coefficient of determination (R^2) varying
304 between 0.80 and 0.95 for SW_{IN} , LW_{IN} , LW_{OUT} and Rn , and between 0.59 and 0.67 for
305 SW_{OUT} , LE and H . The CoSEB model, with the root mean square error (RMSE) of 26.82
306 to 34.25 W/m² and mean absolute error (MAE) of 18.83 to 24.49 W/m² for SW_{IN} , Rn ,
307 LE and H , the RMSE of 12.24 to 17.75 W/m² and the MAE of 8.39 to 13.70 W/m² for

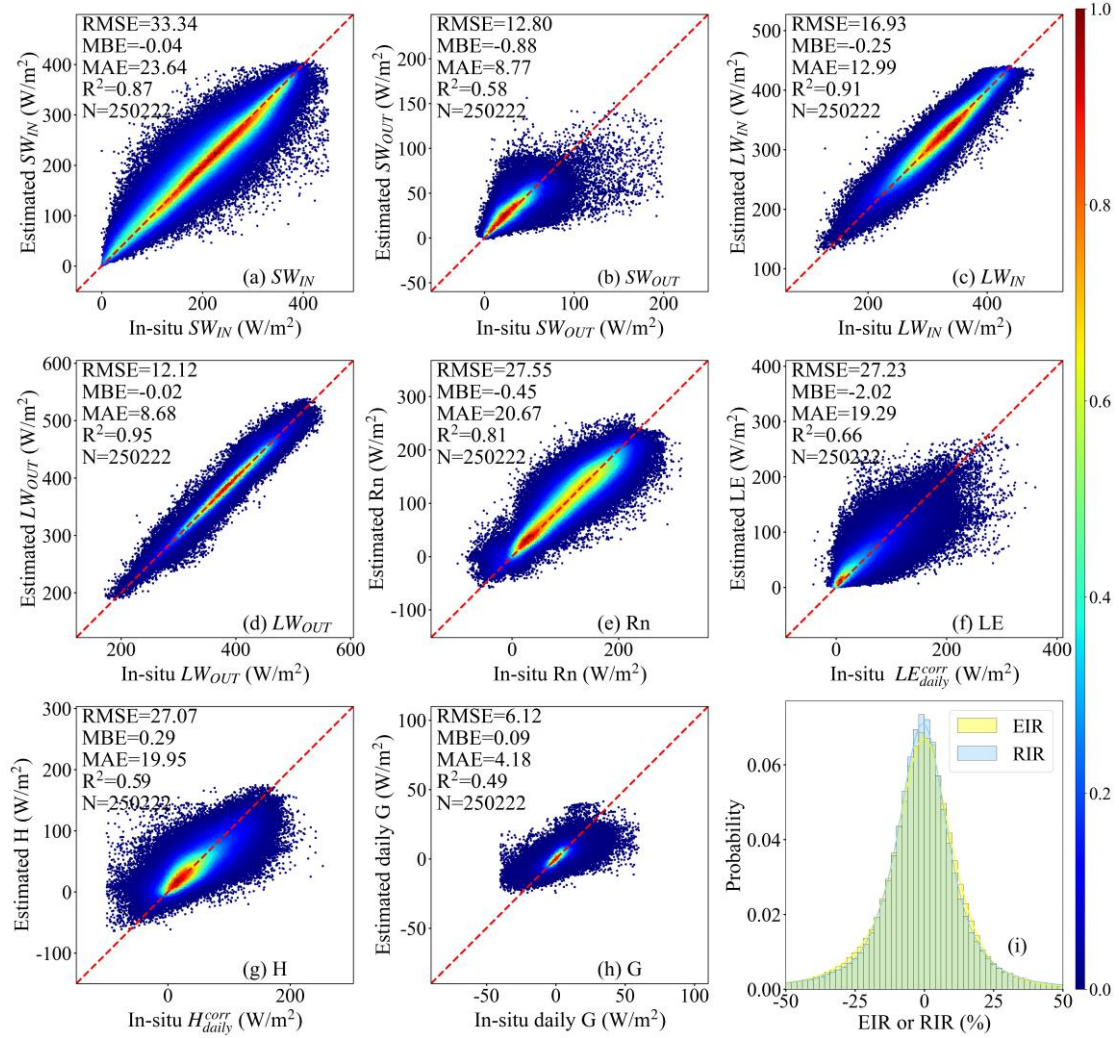
308 SW_{OUT} , LW_{IN} and LW_{OUT} , demonstrated comparable accuracies to the RF-based models,
309 with the RMSE of 27.07 to 33.34 W/m² and MAE of 19.29 to 23.64 W/m² for SW_{IN} ,
310 Rn, LE and H, the RMSE of 12.12 to 16.93 W/m² and the MAE of 8.68 to 12.99 W/m²
311 for SW_{OUT} , LW_{IN} and LW_{OUT} . In the validation of daily G, both the CoSEB and RF-based
312 models yielded RMSEs below 7 W/m². Comparisons with the corresponding training
313 results (Table S3 in the Supplementary Material) indicated that although the CoSEB
314 model performed better on the training datasets, its overall performance remained stable,
315 suggesting that the CoSEB model was not affected by overfitting.

316 Strikingly, the CoSEB model exhibited large superiority in balancing the surface
317 radiation and heat fluxes, with the radiation imbalance ratio [RIR, defined as 100% \times
318 $(SW_{IN} - SW_{OUT} + LW_{IN} - LW_{OUT})/Rn$] and energy imbalance ratio [EIR, defined as 100%
319 $\times (Rn - G - LE - H)/Rn$] of 0, while the RF-based uncoordinated models showed
320 substantial imbalances of the surface radiation and heat fluxes, with RIR and EIR that
321 were approximately normally distributed, having absolute mean values of 38.84% and
322 31.22%, respectively, and reaching as high as 50% in some cases. Furthermore, the RIR
323 as well as EIR tended to be higher under lower solar radiation, air temperature, or FVC,
324 with more frequent low values of these three variables leading to a broader and less
325 peaked distribution of RIR and EIR (see Fig. S1 in the Supplementary Material).



326

327 **Fig. 3** Scatter density plots of the site-based 10-fold cross-validation of daily downward
328 shortwave and longwave radiation (SW_{IN} and LW_{IN}), upward shortwave and longwave
329 radiation (SW_{OUT} and LW_{OUT}), net radiation (Rn), soil heat flux (G), latent heat flux (LE) and
330 sensible heat flux (H) derived by the CoSEB model against in situ observed SW_{IN} , LW_{IN} , SW_{OUT} ,
331 LW_{OUT} , Rn, G, and energy imbalance-corrected LE (LE_{daily}^{corr}) and H (H_{daily}^{corr}). The EIR and RIR
332 in the subfigure (i) represent the energy imbalance ratio and radiation imbalance ratio, which
333 are defined as $100\% \times (Rn - G - LE - H)/Rn$ and $100\% \times (SW_{IN} - SW_{OUT} + LW_{IN} - LW_{OUT})/Rn$,
334 respectively. The colorbar represents the normalized density of data points.



335
336 **Fig. 4 Same as Fig. 3, but for estimates from RF-based uncoordinated models.**

337 **4.1.2 Validation at nine radiation sites from SURFRAD**

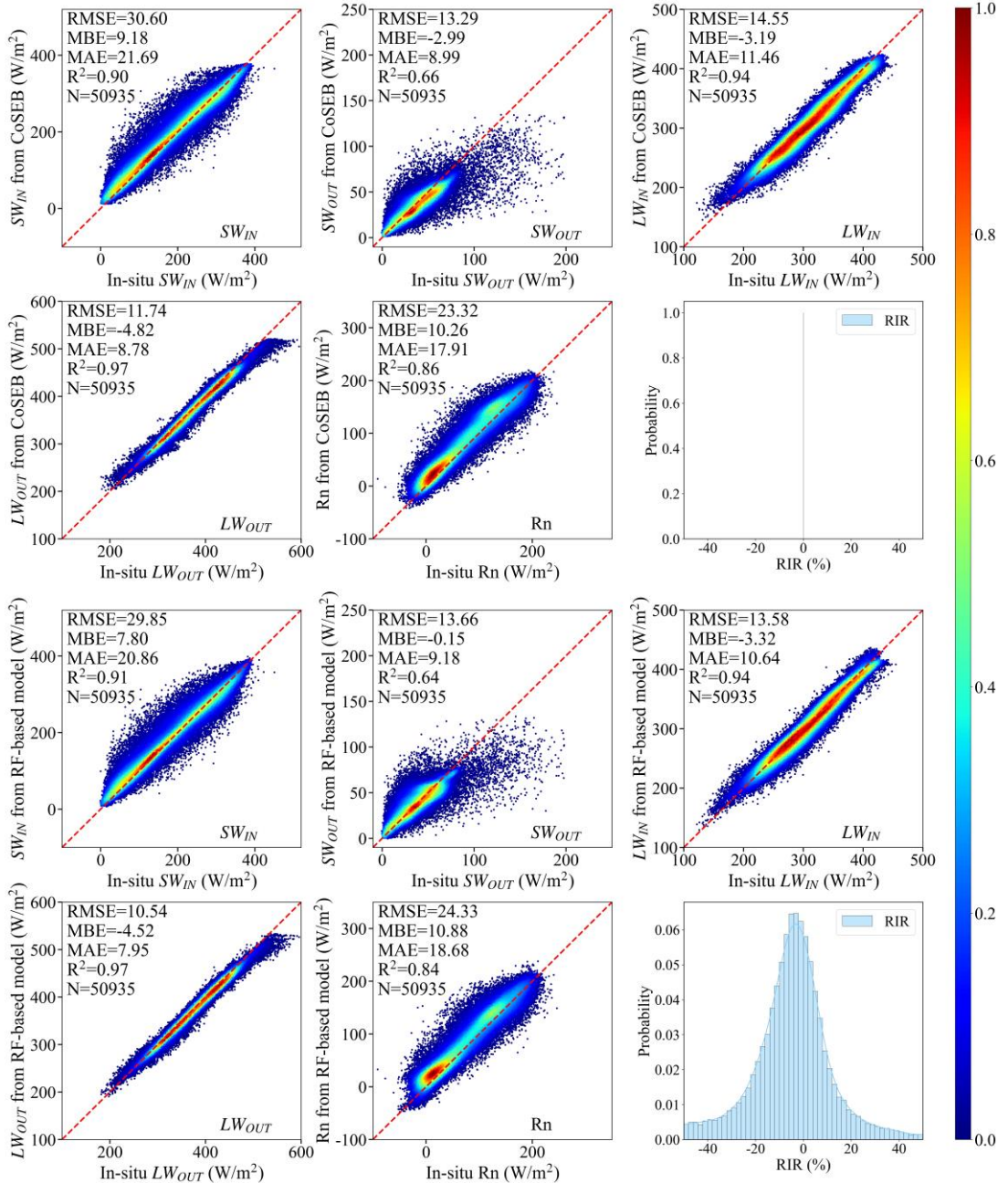
338 To further illustrate the generality and transferability of the renewed CoSEB model,
 339 the validation of estimates of the five radiation components (including SW_{IN} , SW_{OUT} ,
 340 LW_{IN} , LW_{OUT} , Rn) derived from both the CoSEB model and RF-based uncoordinated
 341 models against observations at nine radiation sites from SURFRAD was performed, as
 342 shown in Fig. 5. The results showed that both the CoSEB model and the RF-based
 343 models achieved high accuracy in estimating daily SW_{IN} , SW_{OUT} , LW_{IN} , LW_{OUT} and Rn ,
 344 with the RMSE of $\sim 30 \text{ W/m}^2$ for SW_{IN} , $\sim 14 \text{ W/m}^2$ for SW_{OUT} and LW_{IN} , $\sim 12 \text{ W/m}^2$ for
 345 LW_{OUT} and $\sim 24 \text{ W/m}^2$ for Rn , with the $R^2 > 0.9$ for SW_{IN} , LW_{IN} and LW_{OUT} , ~ 0.65 for
 346 SW_{OUT} and ~ 0.85 for Rn . Compared to the results of the site-based 10-fold cross-
 347 validation at 258 EC sites, the performances at nine radiation sites showed slight

348 improvements, with the RMSE decreasing by 0.74 to 4.54 W/m² for SW_{IN} , LW_{IN} , LW_{OUT}
349 and Rn in the CoSEB model, but a slight degradation with the RMSE increasing by
350 ~ 1.05 W/m² for SW_{OUT} , suggesting the robust performance of the CoSEB model.
351 Furthermore, the CoSEB model demonstrated a large superiority in maintaining surface
352 radiation balance among the five radiation components, with the RIR of 0, in contrast
353 to the RF-based models, which failed to meet this balance, exhibiting significant RIR
354 exceeding 50%.

355 **4.2 Validation and inter-comparisons of the CoSEB-based datasets**

356 As demonstrated in Section 4.1, the renewed CoSEB model with a spatial scale of
357 500 m achieved comparable accuracies to the RF-based uncoordinated models but
358 outperformed them in balancing surface radiation and heat fluxes. Evidenced by the
359 validation for its superiority, the renewed CoSEB model was then applied to the
360 spatially aggregated input datasets to generate our developed global daily datasets with
361 a spatial resolution of 0.05°. To further assess the performance of the developed
362 CoSEB-based datasets, in situ observations from another 44 spatially independent test
363 sites (see Section 2.1), which were not involved in model construction and datasets
364 generation, were used for validation. Mainstream products (i.e. GLASS, BESS-Rad,
365 BESSV2.0, FLUXCOM, PML_V2, MOD16A2 and ETMonitor) were also involved for
366 inter-comparison at the 44 test sites.

367 Note that due to the lack of moderate-resolution global RS-based products/datasets
368 of daily and/or 8-day SW_{OUT} , H and G , the intercomparison between different
369 products/datasets was impossible. Instead, we conducted a validation of these
370 components from the CoSEB-based datasets against in situ observations at 44 test sites,
371 as shown in Figs S2 and S3 in the Supplementary Material. Results indicated that the
372 CoSEB-based datasets could provide good estimates of SW_{OUT} , H and G , with the
373 RMSEs (R^2) of 14.20 W/m² (0.42), 29.75 W/m² (0.44) and 5.69 W/m² (0.44) at daily
374 scale, respectively, and the RMSE (R^2) of 12.19 W/m² (0.39) and 4.60 W/m² (0.47) for
375 8-day SW_{OUT} and G , respectively.



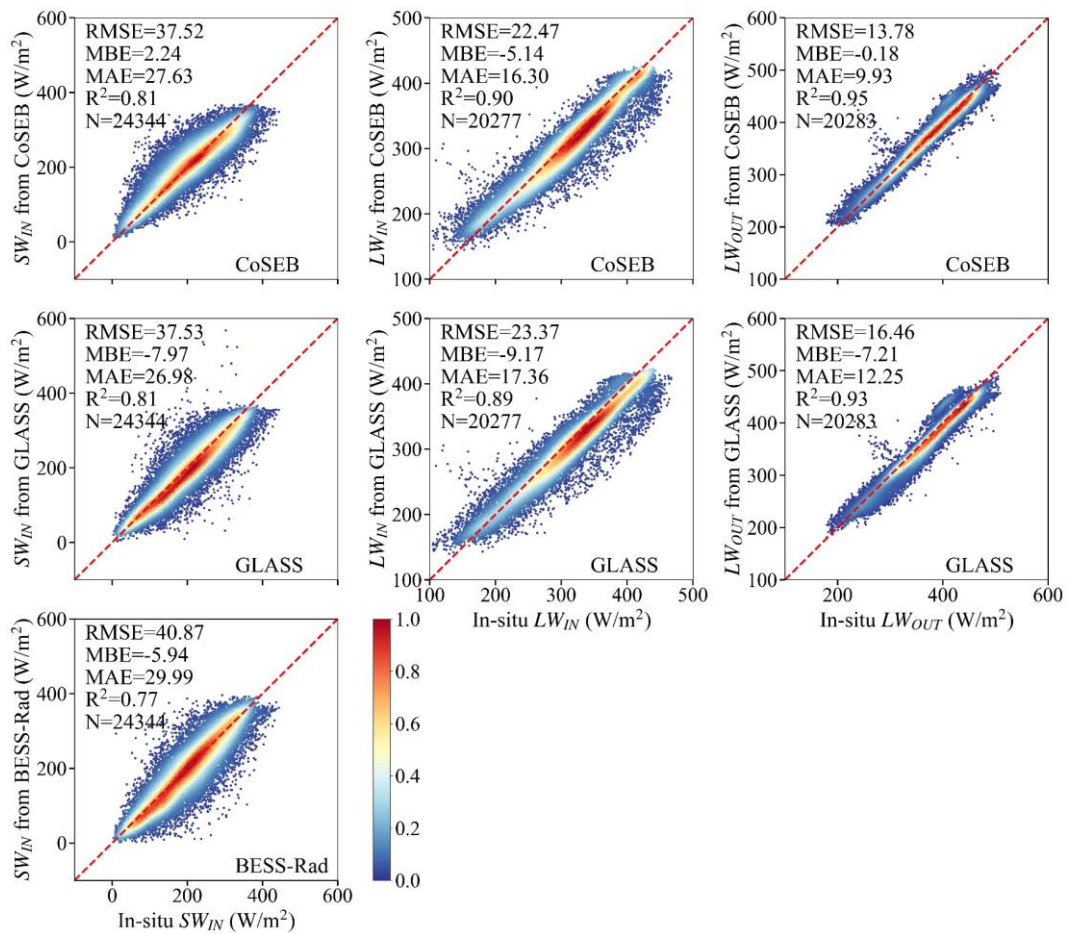
376

377 **Fig. 5 Scatter density plots of the validation of daily downward shortwave and longwave**
 378 **radiation (SW_{IN} and LW_{IN}), upward shortwave and longwave radiation (SW_{OUT} and LW_{OUT})**
 379 **and net radiation (Rn) from the renewed CoSEB model (upper two rows) and RF-based**
 380 **uncoordinated models (lower two rows) against in situ observations at nine radiation sites**
 381 **from SURFRAD. The RIR represents the radiation imbalance ratio, defined as $100\% \times (SW_{IN}$**
 382 **$- SW_{OUT} + LW_{IN} - LW_{OUT})/Rn$. The colorbar represents the normalized density of data points.**

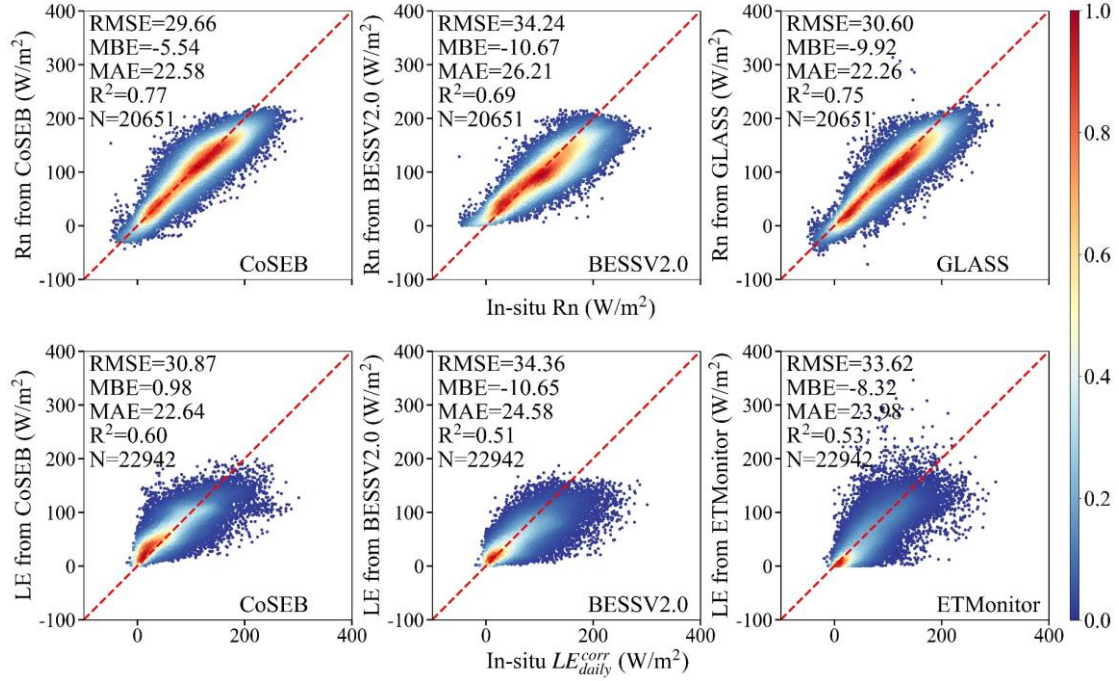
383

Fig. 6 and Fig. 7 present the comparison of daily SW_{IN} , LW_{IN} and LW_{OUT} , as well as Rn and LE from the CoSEB-based datasets and mainstream products/datasets (including GLASS, BESS-Rad, BESSV2.0 and ETMonitor), with in situ observations at 44 test sites, respectively. Overall, the estimates from the CoSEB-based datasets

387 exhibited a closer agreement with in situ observations than those from mainstream
 388 products/datasets, where the CoSEB-based datasets reduced the RMSE by 0.01 W/m²
 389 to 4.58 W/m² and increased the R² by 0.01 to 0.09 compared to mainstream products.
 390 Specifically, the RMSE for the SW_{IN} , LW_{IN} , and LW_{OUT} increased from 37.52 W/m²,
 391 22.47 W/m² and 13.78 W/m² in the CoSEB-based datasets to 37.53 W/m², 23.37 W/m²
 392 and 16.46 W/m² in the GLASS, respectively, and for SW_{IN} from 37.52 W/m² in the
 393 CoSEB-based datasets to 40.87 W/m² in the BESS-Rad. Likewise, the RMSEs for daily
 394 Rn and LE were 29.66 W/m² and 30.87 W/m² in the CoSEB-based datasets, which were
 395 lower than those of 34.24 W/m² and 34.36 W/m² in BESSV2.0, respectively, as well as
 396 those of 30.60 W/m² for Rn in GLASS and 33.62 W/m² for LE in ETMonitor.



397
 398 **Fig. 6 Comparison of the daily downward shortwave radiation (SW_{IN} , the first column),**
 399 **downward longwave radiation (LW_{IN} , the second column) and upward longwave radiation**
 400 **(LW_{OUT} , the third column) from the CoSEB-based datasets, GLASS and BESS-Rad with the**
 401 **in situ observed SW_{IN} , LW_{IN} and LW_{OUT} at 44 test sites. The colorbar represents the normalized**
 402 **density of data points.**



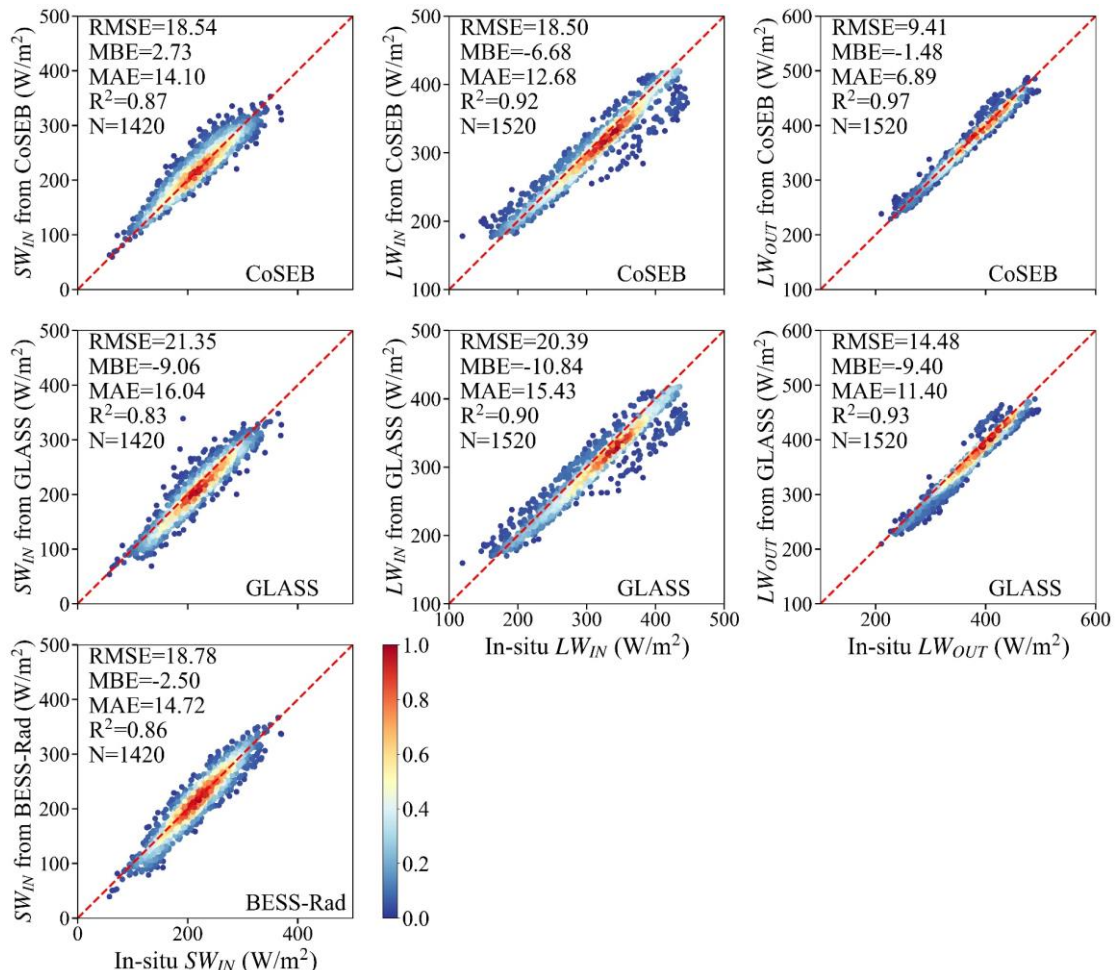
403

404 **Fig. 7 Comparison of the daily net radiation (Rn, the upper row)** and latent heat flux (LE, the
 405 lower row) from the CoSEB-based datasets, BESSV2.0, GLASS and ETMonitor with the in
 406 situ observed Rn, and energy imbalance-corrected LE (LE_{daily}^{corr}) at 44 test sites. The colorbar
 407 represents the normalized density of data points.

408 Figs. 8, 9 and 10 compare the 8-day SW_{IN} , LW_{IN} and LW_{OUT} , Rn and LE, as well as
 409 H from the CoSEB-based datasets and mainstream products, with in situ observations
 410 at 44 test sites, respectively. Overall, the CoSEB-based datasets outperformed the
 411 mainstream products/datasets for all surface radiation and heat fluxes, where the
 412 CoSEB-based datasets reduced the RMSE by 0.24 W/m² to 10.48 W/m² and increased
 413 the R² by 0.01 to 0.38 compared to mainstream products. Specifically, for SW_{IN} , LW_{IN}
 414 and LW_{OUT} , the RMSE increased from 18.54 W/m², 18.50 W/m² and 9.41 W/m² in the
 415 CoSEB-based datasets to 21.35 W/m², 20.39 W/m² and 14.48 W/m² in the GLASS,
 416 respectively, and for SW_{IN} from 18.54 W/m² in the CoSEB-based datasets to 18.78
 417 W/m² in the BESS-Rad. For Rn, the RMSE increased from 19.12 W/m² in the CoSEB-
 418 based datasets to ~23 W/m² in the FLUXCOM and GLASS and to >27 W/m² in the
 419 BESSV2.0, while the R² decreased from 0.82 in the CoSEB-based datasets to 0.75 in
 420 the FLUXCOM and GLASS and to 0.62 in the BESSV2.0. Likewise, for LE, the RMSE
 421 increased from 22.31 W/m² in the CoSEB-based datasets to ~25 W/m² in the

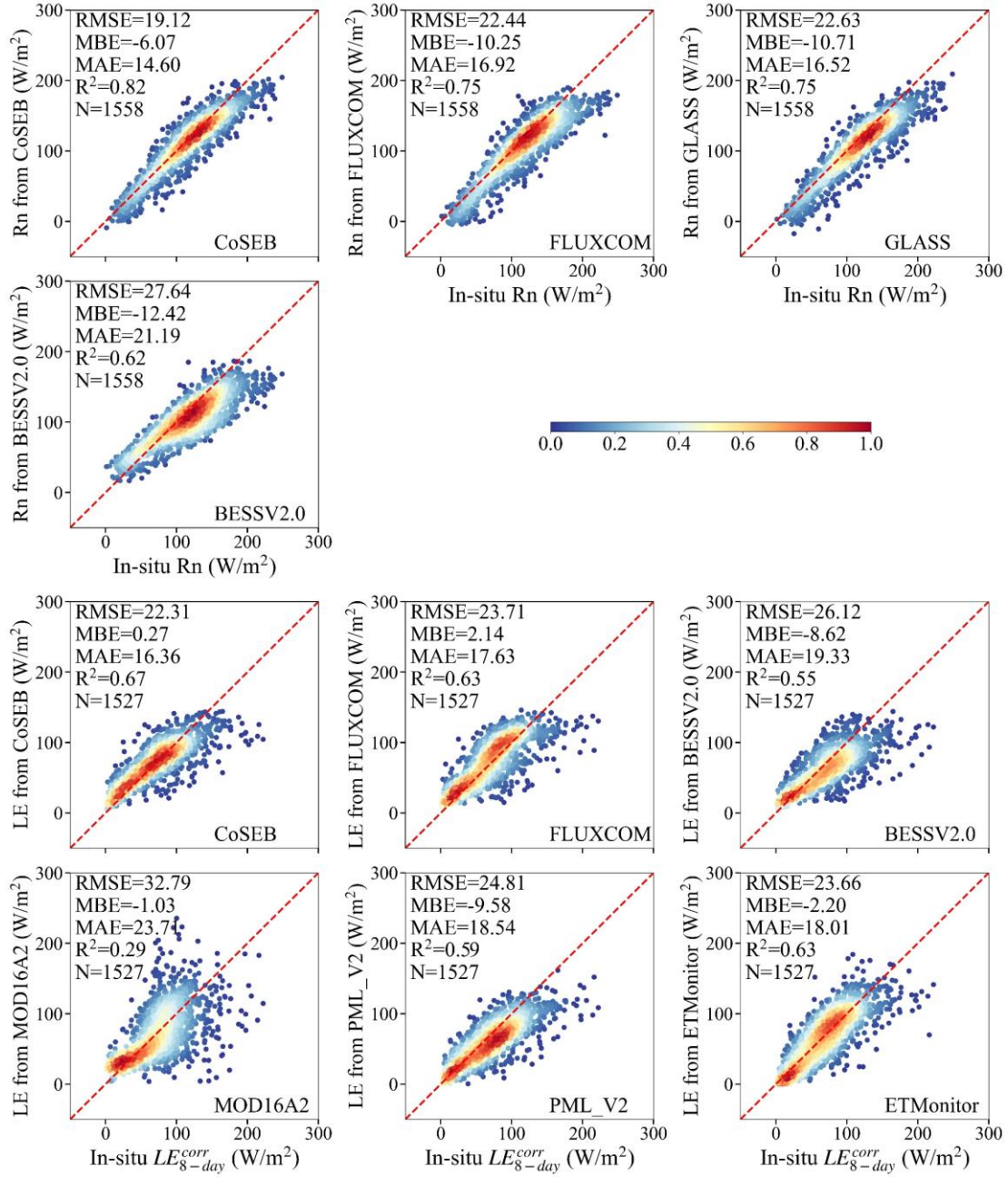
422 FLUXCOM, PML_V2, BESSV2.0 and ETMonitor, and to >32 W/m^2 in MOD16A2,
 423 while the R^2 decreased from 0.67 in the CoSEB-based datasets to ~ 0.60 in the
 424 FLUXCOM, PML_V2, BESSV2.0 and ETMonitor, and to <0.3 in the MOD16A1. For
 425 H, the RMSE increased from 21.63 W/m^2 in the CoSEB-based datasets to 22.64 W/m^2
 426 in the FLUXCOM.

427 The differences between the estimates from the CoSEB-based datasets and
 428 mainstream datasets are likely multifactorial, arising from the simplification and
 429 parameterization uncertainties in physics-based models, as well as the lack of physical
 430 constraints, limited training samples, and incomplete consideration of influencing
 431 factors in other machine-learning-based models.



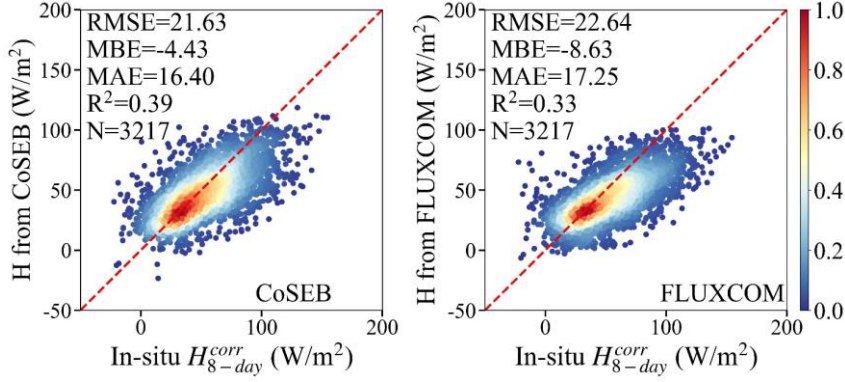
432

433 **Fig. 8 Same as Fig. 6, but for the comparison at 8-day scale.**



434

435 **Fig. 9 Comparison of the 8-day net radiation (Rn, the upper two rows) and latent heat flux**
 436 **(LE, the lower three rows) from the CoSEB-based datasets, FLUXCOM, BESSV2.0, GLASS,**
 437 **MOD16A2, PML_V2 and ETMonitor with in situ observed Rn, and energy imbalance-**
 438 **corrected LE (LE_{8-day}^{corr}) at 44 test sites. The colorbar represents the normalized density of data**
 439 **points.**



440

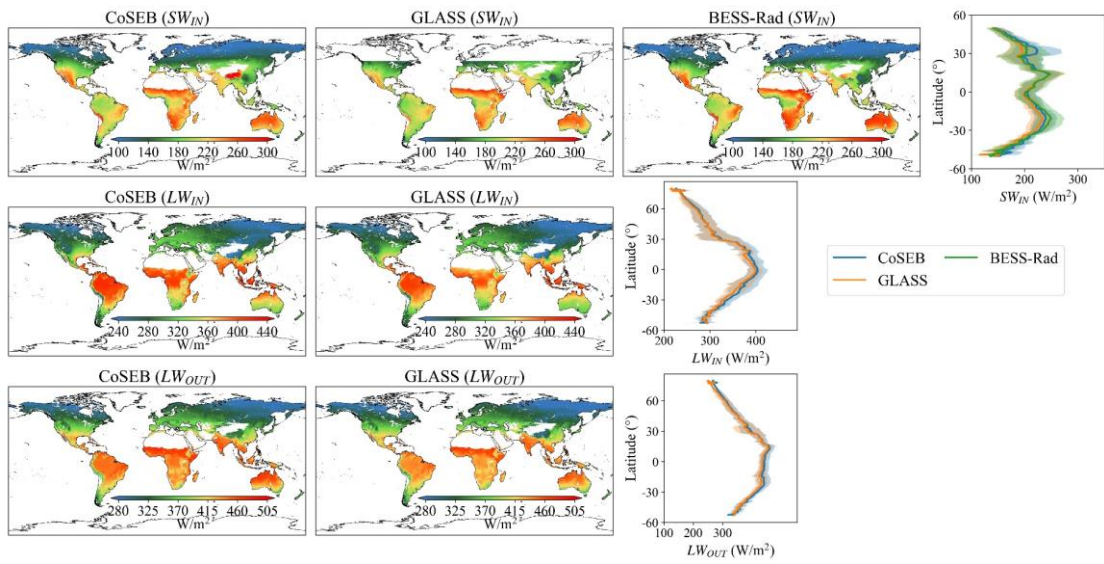
441 **Fig. 10 Comparison of the 8-day sensible heat flux (H) from the CoSEB-based datasets and**
 442 **the FLUXCOM with the in situ energy imbalance-corrected H (H_{8-day}^{corr}) at 44 test sites. The**
 443 **colorbar represents the normalized density of data points.**

444 4.3 Spatial-temporal patterns of global land surface radiation and heat fluxes

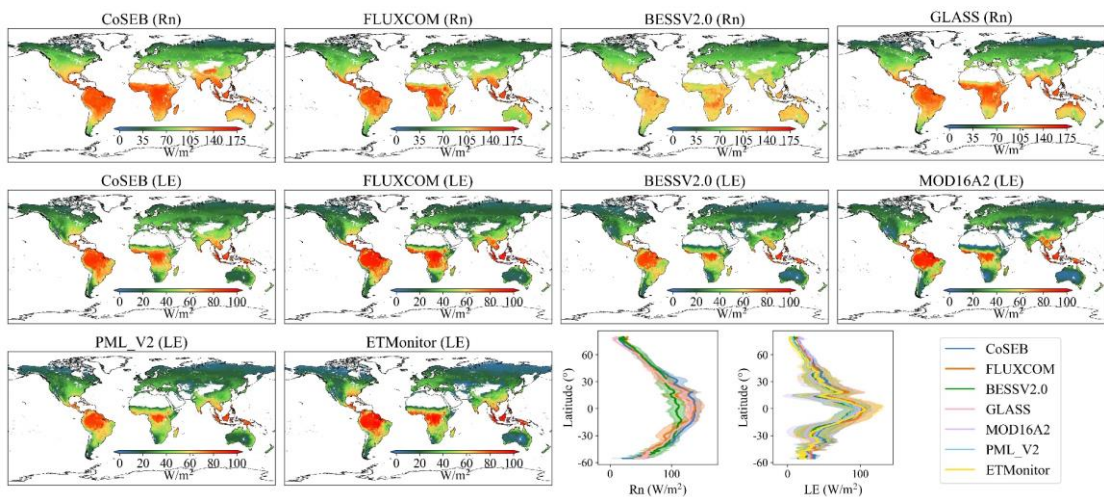
445 In addition to the validation and inter-comparison of the CoSEB-based datasets at
 446 the site scale, we further inter-compared the estimates of land surface radiation and heat
 447 fluxes from the CoSEB-based datasets and the mainstream products/datasets, in terms
 448 of their global spatial and temporal patterns.

449 Figs. 11, 12 and 13 show the spatial distributions (excluding Greenland, Antarctic
 450 continent, deserts, water bodies and permanent snow) and latitudinal profiles of the
 451 global 0.05° mean annual SW_{IN} , LW_{IN} and LW_{OUT} , Rn and LE, as well as H from 2001
 452 to 2018, respectively, as derived from the CoSEB-based datasets and mainstream
 453 products/datasets [i.e. GLASS, BESS-Rad, BESSV2.0, FLUXCOM, MOD16A2,
 454 PML_V2 and ETMonitor, resampled to 0.05° using arithmetic averaging method or
 455 cubic convolutional method if necessary]. Overall, the spatial patterns of the estimates
 456 from the CoSEB-based datasets aligned well with those observed in these mainstream
 457 products/datasets, though regional discrepancies were present. Specifically, the mean
 458 annual LW_{IN} , LW_{OUT} , Rn, and LE generally exhibited decreasing trends from the equator
 459 towards higher latitudes, peaking in regions such as the Amazon Rainforest, Congo
 460 Rainforest, and the Malay Archipelago. In contrast, the higher mean annual SW_{IN} and
 461 H were mainly found in the Tibetan Plateau, southwestern U.S., mid-west Australia,
 462 Sahel and Southern Africa, while the lower values were found in high-latitude regions

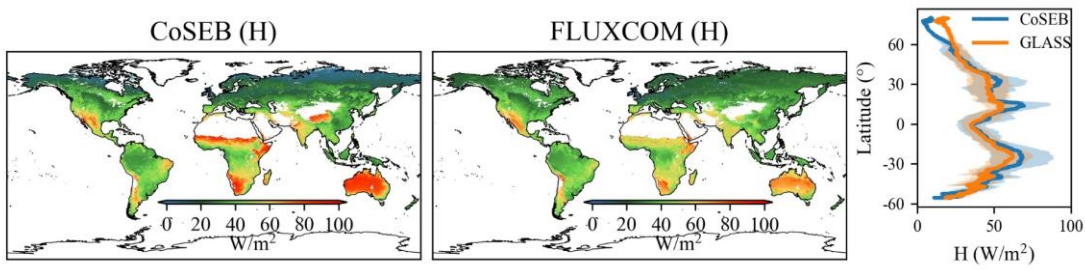
463 of $>50^{\circ}\text{N}$. In the region with high values, the mean annual estimates of SW_{IN} from the
464 CoSEB-based datasets were higher than those from GLASS but lower than those from
465 BESS-Rad, the estimates of LW_{IN} and LW_{OUT} from the CoSEB-based datasets were both
466 higher than those from GLASS, the estimates of Rn from the CoSEB-based datasets
467 were significantly higher than those from BESSV2.0, and comparable to or slightly
468 higher than those from FLUXCOM and GLASS, the estimates of LE from the CoSEB-
469 based datasets were close to those from BESSV2.0 and PML_V2, but slightly lower
470 than those from FLUXCOM, MOD16A2 and ETMonitor. Besides, the estimates of H
471 from the CoSEB-based datasets were higher than those from FLUXCOM in regions
472 with high values, while lower than those from FLUXCOM in regions with low values.



473
 474 **Fig.11 Spatial patterns of global mean annual downward shortwave radiation (SW_{IN} , the first**
 475 **row), downward longwave radiation (LW_{IN} , the second row) and upward longwave radiation**
 476 **(LW_{OUT} , the third row) from 2001 to 2018 by CoSEB-based datasets, GLASS and BESS-Rad.**
 477 **The rightmost subfigure of each row represents the latitudinal profiles of mean annual SW_{IN} ,**
 478 **LW_{IN} and LW_{OUT} from CoSEB-based datasets, GLASS and BESS-Rad, where the shaded area**
 479 **represents the variation of standard deviation for each product.**



480
 481 **Fig.12 Spatial patterns of global mean annual net radiation (Rn , the first row) and latent heat**
 482 **flux (LE , the second and third rows) from 2001 to 2018 by CoSEB-based datasets, FLUXCOM,**
 483 **BESSV2.0, MOD16A2, PML_V2, ETMonitor and GLASS. The last two subfigures of the third**
 484 **row represent the latitudinal profiles of mean annual Rn and LE from CoSEB-based datasets**
 485 **and these mainstream products/datasets, where the shaded area represents the variation of**
 486 **standard deviation for each product.**

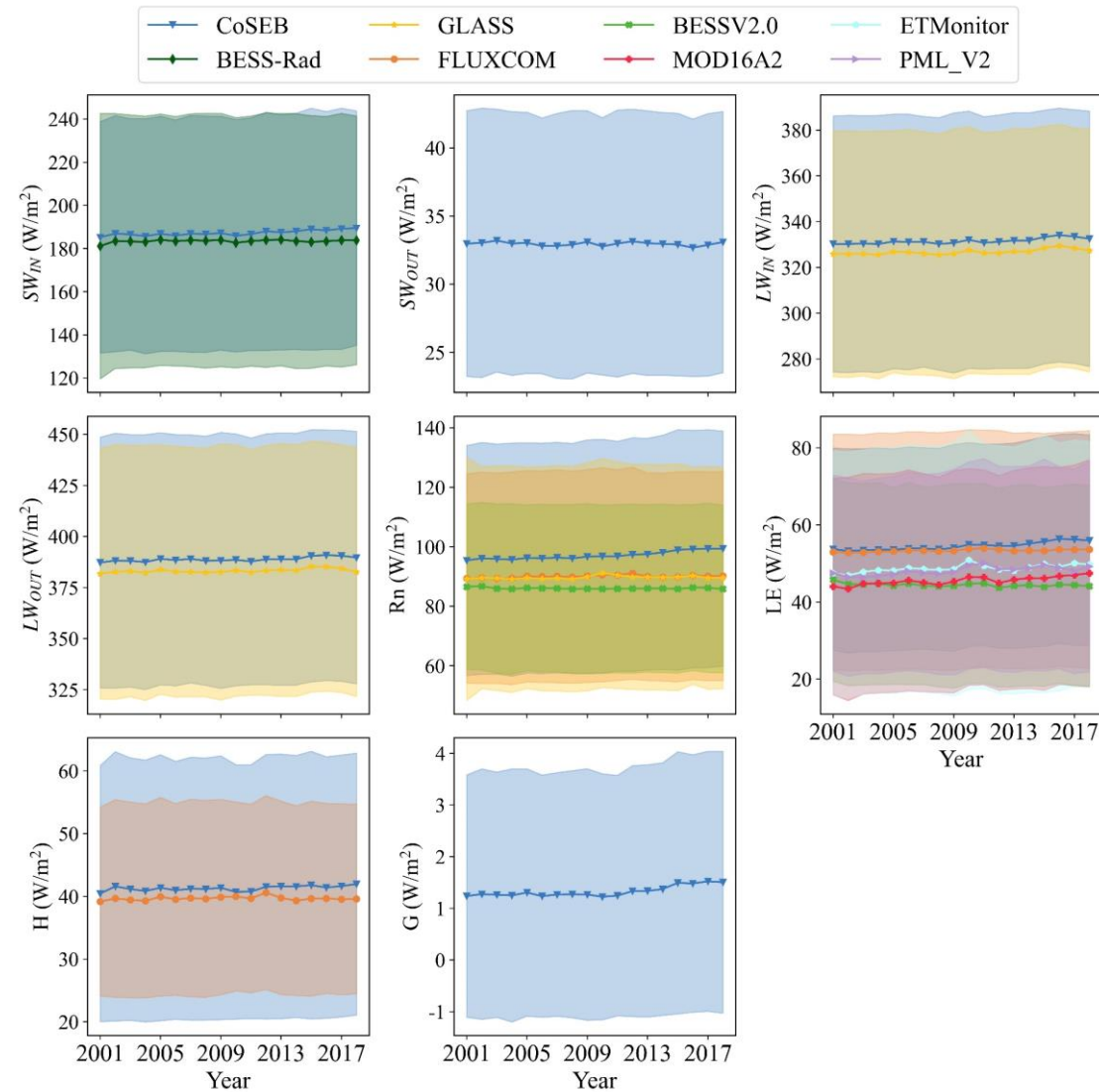


487

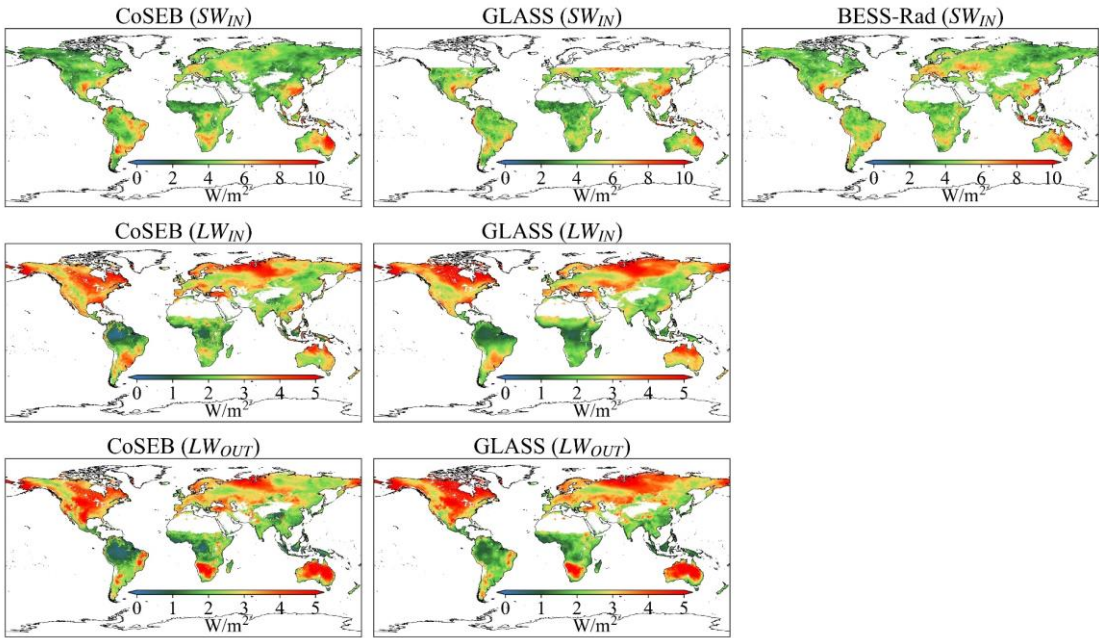
488 **Fig.13 Spatial patterns of global mean annual sensible heat flux (H) from 2001 to 2018 by**
 489 **CoSEB-based datasets and FLUXCOM. The rightmost subfigure represents the latitudinal**
 490 **profiles of mean annual H from CoSEB-based datasets and FLUXCOM, where the shaded**
 491 **area represents the variation of standard deviation for each product.**

492 The temporal evolutions of the global (excluding Greenland, Antarctic continent,
 493 deserts, water bodies and permanent snow) land surface radiation and heat fluxes
 494 derived from the CoSEB-based datasets and mainstream products/datasets from 2001
 495 to 2018 were also investigated, as shown in Fig. 14. The results indicated that the
 496 temporal variation of each flux from the CoSEB-based datasets generally agreed well
 497 with those from mainstream products/datasets, *exhibiting relatively stable trends*. The
 498 global annual mean estimates using area weighting average by the CoSEB-based
 499 datasets from 2001 to 2018 varied between ~ 185.22 and ~ 189.50 W/m^2 with the mean
 500 of ~ 187.23 W/m^2 for SW_{IN} , between ~ 32.67 and ~ 33.20 W/m^2 with the mean of ~ 32.96
 501 W/m^2 for SW_{OUT} , between ~ 330.24 and ~ 334.14 W/m^2 with the mean of ~ 331.50 W/m^2
 502 for LW_{IN} , between ~ 387.25 and ~ 390.82 W/m^2 with the mean of ~ 388.81 W/m^2 for
 503 LW_{OUT} , between ~ 95.41 and ~ 99.39 W/m^2 with the mean of 97.11 W/m^2 for Rn ,
 504 between ~ 53.24 and ~ 56.37 W/m^2 with the mean of ~ 54.53 W/m^2 for LE , between
 505 ~ 40.44 and ~ 41.96 W/m^2 with the mean of ~ 41.29 W/m^2 for H , and between ~ 1.22 and
 506 ~ 1.52 W/m^2 with the mean of ~ 1.33 W/m^2 for G . For each radiation or heat flux, the
 507 annual mean estimates from the CoSEB-based datasets were overall higher than those
 508 from the mainstream products/datasets. In particular, the annual mean Rn estimates
 509 from the CoSEB-based datasets were higher than those from FLUXCOM, GLASS and
 510 BESSV2.0 sequentially, and the annual mean LE estimates from the CoSEB-based
 511 datasets were marginally higher than those from FLUXCOM, but substantially
 512 exceeded those from ETMonitor, PML_V2, MOD16A2 and BESSV2.0 sequentially.

513 The anomaly-based analyses (Fig. S4 in the Supplementary Material) reveal clear and
 514 coherent temporal trends of these radiation and heat fluxes, which respond well to
 515 global climate change, such as increasing atmospheric CO₂ and rising air temperatures.



517
 518 **Fig. 14 Temporal variation of annual mean downward shortwave radiation (SW_{in}), upward**
 519 **radiation (SW_{out}), downward longwave radiation (LW_{in}), upward longwave**
 520 **radiation (LW_{out}), net radiation (Rn), latent heat flux (LE), sensible heat flux (H) and soil heat**
 521 **flux (G) from 2001 to 2018 from the CoSEB-based datasets, BESS-Rad, GLASS, FLUXCOM,**
 522 **BEVV2.0, PML_V2, MOD16A2 and ETMonitor. The shaded area represents the variation of**
 523 **the standard deviation for each product.**

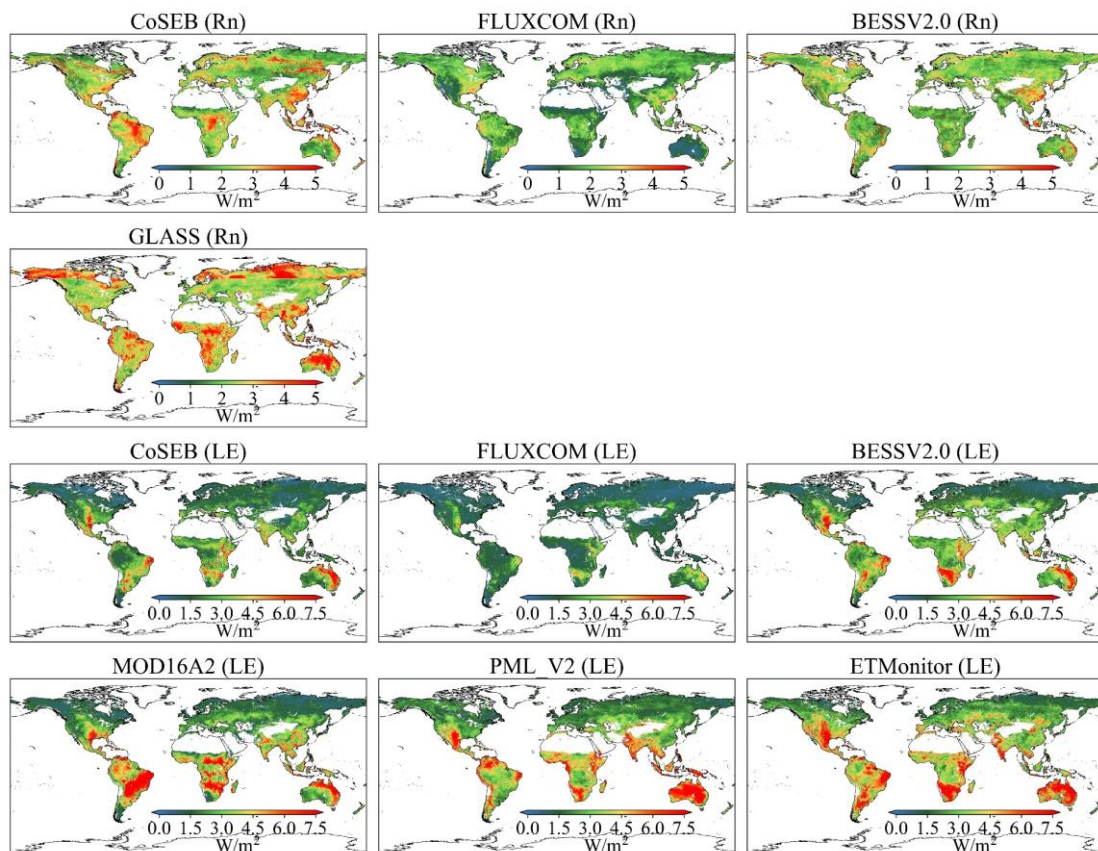


524

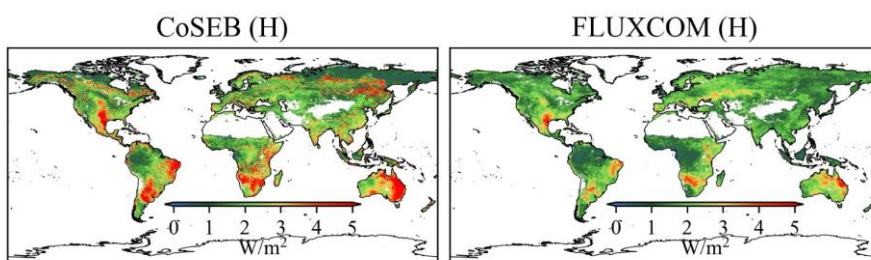
525 **Fig. 15 Spatial distribution of interannual variability (standard deviation) of downward**
 526 **shortwave radiation (SW_{IN} , the first row), downward longwave radiation (LW_{IN} , the second**
 527 **row) and upward longwave radiation (LW_{OUT} , the third row) from 2001 to 2018 by the CoSEB-**
 528 **based datasets, GLASS and BESS-Rad.**

529 Figs. 15, 16 and 17 show the spatial patterns (excluding Greenland, Antarctic
 530 continent, deserts, water bodies and permanent snow) of interannual variability of SW_{IN} ,
 531 LW_{IN} and LW_{OUT} , Rn and LE, as well as H from 2001 to 2018, respectively, derived
 532 from the CoSEB-based datasets and mainstream products/datasets. In general, the
 533 estimates from the CoSEB-based datasets displayed similar interannual variability in
 534 space with those from the mainstream products/datasets. Specially, the estimates of
 535 SW_{IN} from the CoSEB-based datasets, BESS-Rad, and GLASS exhibited a significant
 536 interannual variability mainly in northeastern Australia, eastern South America,
 537 Southeast China, and Southwest North America. The interannual variability of LW_{IN}
 538 and LW_{OUT} by the CoSEB-based datasets and GLASS displayed high values primarily
 539 at middle-to-high latitudes of the Northern Hemisphere and parts of Africa and
 540 Australia. The interannual variability of Rn observed by the CoSEB-based datasets was
 541 generally lower than that of GLASS, but higher than that of BESSV2.0 and FLUXCOM.
 542 The CoSEB-based datasets missed the strong interannual variability of LE as observed
 543 in MOD16A2, PML_V2 and ETMonitor in parts of Africa, Australia and eastern South

544 America. Furthermore, FLUXCOM exhibited the weakest interannual variability of LE
 545 in almost all regions. The interannual variability of H derived from the CoSEB-based
 546 datasets was higher than that from FLUXCOM, with stronger interannual variabilities
 547 mainly observed in parts of eastern South America, southern Africa, and northeastern
 548 Australia.



549
 550 **Fig. 16 Spatial distribution of interannual variability (standard deviation) of net radiation (Rn,**
 551 **the first and second rows) and latent heat flux (LE, the third and fourth rows) from 2001 to**
 552 **2018 by the CoSEB-based datasets, FLUXCOM, BESSV2.0, MOD16A2, PML_V2,**
 553 **ETMonitor and GLASS.**



554
 555 **Fig. 17 Spatial distribution of interannual variability (standard deviation) of sensible heat flux**
 556 **(H) from 2001 to 2018 by the CoSEB-based datasets and FLUXCOM.**

557 **5 Discussion**

558 Accurately monitoring the spatial and temporal variations of global land surface
559 radiation and heat fluxes is crucial for quantifying the exchange of radiation, heat and
560 water between the land and atmosphere under global climate change (Chen et al., 2020;
561 Du et al., 2024; Kim et al., 2023; Liang et al., 2006; Wang et al., 2020). However,
562 although numerous global RS-based products/datasets of land surface radiation and
563 heat fluxes have been developed using physical and/or statistical methods, they
564 typically provide either merely a single flux or multiple fluxes (see Table 1) that are
565 estimated separately from uncoordinated models (Huang et al., 2024; Jung et al., 2019;
566 Sun et al., 2023; Tang et al., 2019), leading to noticeable radiation imbalance and/or
567 heat imbalance when these products are combined for practical applications. To address
568 these limitations, we generated high-accuracy global datasets of land surface radiation
569 and heat fluxes from 2000 to 2020 that adhere to both radiation and heat conservation
570 laws, using our proposed CoSEB model (Wang et al., 2025).

571 Our CoSEB model, integrating underlying physical principles of training datasets
572 into machine learning technique to effectively learn the interrelations among multiple
573 targeted outputs, was originally designed for coordinating estimates of global land
574 surface energy balance components (Rn, LE, H and G) to satisfy the energy
575 conservation (Wang et al., 2025). Inspired by the idea of constructing the original
576 CoSEB model, we further incorporated land surface radiation fluxes into our model to
577 simultaneously consider the physical constraints of both surface radiation and heat
578 conservation principles, by renewing the CoSEB using multiple remote sensing and
579 reanalysis datasets, as well as in-situ observations of SW_{IN} , SW_{OUT} , LW_{IN} , LW_{OUT} , Rn,
580 LE, H and G. In selecting the 19 input variables to accommodate the additional target
581 variables, prior knowledge derived from previous studies was employed to identify
582 factors that exert significant influence on surface radiation and heat flux while
583 maintaining relative inter-independence as much as possible (Jung et al., 2019; Mohan
584 et al., 2020; Wang et al., 2021; Xian et al., 2024). This practice is commonly adopted

585 in data-driven models for estimating land surface water, energy, and carbon fluxes (Bai
586 et al., 2024; Elghawi et al., 2023; Han et al., 2023; O. & Orth, 2021). The importance
587 scores of the 19 different feature variables are exhibited in Table S4 in the
588 Supplementary Material, and downward solar radiation, the primary source of the
589 energy at the earth surface, is the most important input variable, consistent with the
590 results from our previous study (Wang et al., 2025). Although some of the selected
591 variables may exhibit a certain degree of multi-collinearity, each contributes unique and
592 physically meaningful information, supporting the inclusion of all variables in model
593 construction. Note that the variable importance, derived from the built-in method of the
594 random forests and potentially affected by multicollinearity among the input variables,
595 is presented only as a reference. Retaining all 19 feature variables ensures the model's
596 flexibility and generalization capability, enabling future incorporation of additional
597 representative ground-based observations for further training and improvement.
598 Besides, to investigate the impact of lagged effects of input variables on model
599 performance, experiments were also conducted by adding lagged variables (e.g., the air
600 temperature of the previous day) to the 19 input features. The results (Fig. [S4-S5](#) in the
601 Supplementary Material) showed almost no improvement in model accuracy,
602 suggesting that lagged effects on model performance were negligible within the CoSEB
603 framework for estimates of daily surface radiation and heat fluxes. Furthermore, to
604 better illustrate the effect of including additional radiation components (SW_{IN} , SW_{OUT} ,
605 LW_{IN} and LW_{OUT}) in the renewed CoSEB model compared with the original version by
606 Wang et al. (2025), we have tested the performance of a reconstructed model that
607 estimated only Rn, LE, H and G using the same independent variables and samples as
608 those in the renewed CoSEB model. The results (Fig. [S5-S6](#) in the supplementary
609 material) showed no significant differences in accuracy compared with those of the
610 renewed CoSEB model, indicating the expansion of radiation components did not
611 compromise model performance.

612 The main advantages of our CoSEB-based datasets of land surface radiation and

heat fluxes lie in that [1] they are the first data-driven global datasets that satisfy both surface radiation balance ($SW_{IN} - SW_{OUT} + LW_{IN} - LW_{OUT} = Rn$) and heat balance ($LE + H + G = Rn$) among the eight fluxes, as demonstrated by both the RIR and EIR of 0, [2] the radiation and heat fluxes are characterized by high accuracies when validated against in-situ measurements at 44 independent test sites (see the second paragraph in Section 2.1), where (1) the RMSEs for daily estimates of SW_{IN} , SW_{OUT} , LW_{IN} , LW_{OUT} , Rn , LE , H and G from the CoSEB-based datasets were 37.52 W/m^2 , 14.20 W/m^2 , 22.47 W/m^2 , 13.78 W/m^2 , 29.66 W/m^2 , 30.87 W/m^2 , 29.75 W/m^2 and 5.69 W/m^2 , respectively, as well as for 8-day estimates were 18.54 W/m^2 , 12.19 W/m^2 , 18.50 W/m^2 , 9.41 W/m^2 , 19.12 W/m^2 , 22.31 W/m^2 , 21.63 W/m^2 and 4.60 W/m^2 , respectively, (2) the CoSEB-based datasets, in comparison to the mainstream RS-based products/datasets (i.e. GLASS, BESS-Rad, FLUXCOM, BESSV2.0, MOD16A2, PML_V2 and ETMonitor), better agreed with the in situ observations at the 44 test sites, showing the RMSE reductions ranging from 0.01 W/m^2 to 4.58 W/m^2 for SW_{IN} , LW_{IN} , LW_{OUT} , Rn and LE at daily scale, and 0.24 W/m^2 to 10.48 W/m^2 for SW_{IN} , LW_{IN} , LW_{OUT} , Rn , LE and H at 8-day scale. Furthermore, the CoSEB-based datasets outperformed the ERA5-Land reanalysis datasets in estimating surface energy fluxes (where SW_{OUT} , LW_{OUT} , Rn and G for the ERA5-Land were inferred from surface radiation balance and heat balance), particularly for SW_{OUT} , H and G , with RMSE reductions of $0.13\text{--}8.15 \text{ W/m}^2$ when validated against in situ observations at the 44 test sites (Figs. [S6](#)[S7](#) and [S7](#)[S8](#) in the Supplementary Material). [Preliminary analysis indicates that the CoSEB-based datasets exhibit spatial patterns consistent with those of mainstream RS-based datasets and Earth system model outputs \(see Fig. S9 in the supplementary material\), suggesting that the CoSEB-based datasets \(or CoSEB framework\) more broadly, are capable of reproducing the large-scale spatial features of Earth system models. This capability would be a great benefit to the community given the limitations associated with the high computational cost and long execution time of Earth system models. More detailed analysis about their similarities and differences can be further conducted in future](#)

641 ~~work. Preliminary analysis indicates that the CoSEB-based datasets exhibit spatial~~
642 ~~patterns consistent with those of mainstream RS-based datasets and Earth system model~~
643 ~~outputs (see Fig. S8 in the supplementary material). More detailed analysis about their~~
644 ~~similarities and differences can be further conducted in future work.~~

645 Our developed datasets could be potentially applied in many fields, including but
646 not limited to (1) exploring the spatial-temporal patterns of global land surface radiation
647 and heat flux (es) and their driving mechanisms over the past decades under global
648 change (e.g., rising CO₂ concentration, greening land surface and increasing air
649 temperature), (2) investigating the variability of land surface radiation and heat fluxes
650 caused by extreme events and human activities, e.g. afforestation or deforestation,
651 wildfire, air pollution, weather extremes and urbanization, (3) assessing the resources
652 of solar energy, geothermal energy, surface and ground water at regional and global
653 scales, (4) monitoring natural hazards, e.g. drought in agriculture and forestry.

654 The uncertainties of our datasets are relevant to (1) the data preprocessing, and (2)
655 the application of the CoSEB model across different spatial scales. Specifically, daily
656 averages of surface radiation and heat fluxes for each day were obtained for analysis
657 from good-quality half-hourly observations when the fraction of these good-quality
658 half-hourly observations was greater than 80% in a day, due to the lack of consensus on
659 the method for aggregating gapped half-hourly observations to daily data (Tang et al.,
660 2024a; Yao et al., 2017; Zheng et al., 2022). Simple temporal interpolation of half-
661 hourly in situ observations, which could therefore introduce substantial uncertainties,
662 was not applied, because surface radiation and heat fluxes are sensitive to short-term
663 variations in meteorological conditions and their intraday dynamics are often complex.
664 Likewise, since there was no agreement on how to correct for the energy imbalance of
665 turbulent heat fluxes, we adopted the most widely applied Bowen ratio method to
666 enforce energy closure between $Rn - G$ and $LE + H$ (Castelli et al., 2018; Twine et
667 al., 2000; Zhang et al., 2021). Another potential source of uncertainty arises from
668 differences in meteorological reanalysis data caused by spatial downscaling, which, as

669 demonstrated in our previous study (Wang et al., 2025, the last paragraph of Section
670 5.1), has a relatively small impact on model estimates by the machine-learning-based
671 CoSEB model combined with finer-resolution surface-related variables that partially
672 compensate for the spatial heterogeneity and localized variations not captured by the
673 coarse-resolution datasets. These data preprocessing had an effect on the construction
674 of the renewed CoSEB model, which may further affect the global datasets. Moreover,
675 the renewed CoSEB model was constructed at the spatial scale of 500 m to match the
676 footprints of the in situ EC observations, but applied at the spatial resolution of 0.05°
677 to generate global datasets, mainly limited by the computing and storage capabilities of
678 our personal computers. However, the CoSEB-based datasets have also been validated
679 and inter-compared at 44 independent test sites to demonstrate that the difference in
680 spatial scale would not much affect the performance of the datasets. Note that the 302
681 sites used for training, validation, and testing are predominantly located in the Northern
682 Hemisphere, reflecting the inherent uneven distribution of the global flux networks.
683 Although these sites cover a wide range of land cover types and climate regimes,
684 thereby providing substantial heterogeneity for model development, the limited
685 representation of the Southern Hemisphere may introduce uncertainties in the
686 estimation of surface radiation and heat fluxes for certain ecosystems and soil types. In
687 the future, enhancing the flux observation network coverage in the Southern
688 Hemisphere, particularly in South America and Africa, and incorporating these
689 observations into the CoSEB framework would help further improve the accuracy of
690 surface radiation and heat flux estimates in these regions. Furthermore, the radiation
691 and heat balance in this study refers specifically to the conservation among the eight
692 variables (i.e., SW_{IN} , LW_{IN} , SW_{OUT} , LW_{OUT} , Rn , LE , G , H), which constitute the major
693 components of the surface energy budget, and does not account for energy introduced
694 by disturbance-related processes such as wildfires and volcanic eruptions. Despite these
695 these uncertainties, it is worth emphasizing that our work was the first attempt to
696 innovatively develop data-driven energy-conservation datasets of global land surface

697 radiation and heat fluxes with high accuracies.

698 **6 Data availability**

699 The energy-conservation datasets of global land surface radiation and heat fluxes
700 generated by the CoSEB model with spatial-temporal resolutions of daily and 0.05°
701 from Feb.26, 2000 to Dec.31, 2020 are freely available through the National Tibetan
702 Plateau Data Center at <https://doi.org/10.11888/Terre.tpdc.302559> (Tang et al., 2025a)
703 and through the Science Data Bank (ScienceDB) at
704 <https://doi.org/10.57760/sciencedb.27228> (Tang et al., 2025b).

705 **7 Summary and Conclusion**

706 This study for the first time developed data-driven energy-conservation datasets
707 of global land surface radiation and heat fluxes using our CoSEB model renewed based
708 on GLASS and MODIS products, ERA5-Land reanalysis datasets, topographic data,
709 CO₂ concentration data, and observations at 258 EC sites worldwide.

710 The CoSEB-based datasets of land surface radiation and heat fluxes are the first
711 data-driven global datasets that satisfy both surface radiation balance ($SW_{IN} - SW_{OUT} +$
712 $LW_{IN} - LW_{OUT} = Rn$) and heat balance ($LE + H + G = Rn$) among the eight fluxes.
713 Meanwhile, the CoSEB-based datasets outperformed the mainstream products/datasets
714 in accuracy. Specifically, at 44 independent test sites, the RMSEs (R^2) for daily
715 estimates of SW_{IN} , SW_{OUT} , LW_{IN} , LW_{OUT} , Rn , LE , H and G from the CoSEB-based
716 datasets were 37.52 W/m^2 (0.81), 14.20 W/m^2 (0.42), 22.47 W/m^2 (0.90), 13.78 W/m^2
717 (0.95), 29.66 W/m^2 (0.77), 30.87 W/m^2 (0.60), 29.75 W/m^2 (0.44) and 5.69 W/m^2 (0.44),
718 respectively, as well as for 8-day estimates were 18.54 W/m^2 (0.87), 12.19 W/m^2 (0.39),
719 18.50 W/m^2 (0.92), 9.41 W/m^2 (0.97), 19.12 W/m^2 (0.82), 22.31 W/m^2 (0.67), 21.63
720 W/m^2 (0.39) and 4.60 W/m^2 (0.47), respectively. Moreover, the estimates from the
721 CoSEB-based datasets in comparison to those from the mainstream products/datasets
722 reduced the RMSE by 0.01 W/m^2 to 4.58 W/m^2 and increased the R^2 by 0.01 to 0.09
723 for SW_{IN} , LW_{IN} , LW_{OUT} , Rn and LE at daily scale, and reduced the RMSE by 0.24 W/m^2

724 to 10.48 W/m^2 and increased the R^2 by 0.01 to 0.38 for SW_{IN} , LW_{IN} , LW_{OUT} , Rn , LE and
725 H at 8-day scale, when these estimates were validated against in situ observations at 44
726 independent test sites. Furthermore, the CoSEB-based datasets effectively captured the
727 spatial-temporal variability of global land surface radiation and heat fluxes, aligning
728 well with those from the mainstream products.

729 Our developed datasets hold significant potential for application across diverse
730 fields such as agriculture, forestry, hydrology, meteorology, ecology, and environmental
731 science. They can facilitate comprehensive studies on the variability, impacts, responses,
732 adaptation strategies, and mitigation measures of global and regional land surface
733 radiation and heat fluxes under the influences of climate change and human activities.
734 These datasets will provide valuable insights and data support for scientific research,
735 policy-making, and environmental management, advancing global solutions to address
736 climate change.

737 **Author contribution**

738 JW: Writing – original draft, Visualization, Software, Formal analysis, Data
739 curation. RT: Writing – original draft, Validation, Supervision, Methodology, Funding
740 acquisition, Formal analysis, Conceptualization. ML: Writing – review & editing,
741 Validation. ZL: Writing – review & editing.

742 **Competing interests**

743 The authors declare that they have no conflict of interest.

744 **Acknowledgment**

745 We thank the work from the AmeriFlux, FLUXNET, EuroFlux, OzFlux,
746 ChinaFLUX, the National Tibetan Plateau/Third Pole Environment Data Center and
747 SURFRAD for providing in situ measurements. We would also like to thank Dr. Martin
748 Jung and Dr. Ulrich Weber for providing the FLUXCOM Bowen ratio-corrected
749 products. This work is supported by the National Natural Science Foundation of China

750 [42271378], and the Strategic Priority Research Program of the Chinese Academy of
751 Sciences (Grant No. XDB0740202).

752 References

753 Bai, Y., Mallick, K., Hu, T., Zhang, S., Yang, S. and Ahmadi, A.: Integrating machine
754 learning with thermal-driven analytical energy balance model improved
755 terrestrial evapotranspiration estimation through enhanced surface conductance,
756 *Remote Sens. Environ.*, 311, 114308. 10.1016/j.rse.2024.114308, 2024.

757 Bartkowiak, P., Ventura, B., Jacob, A. and Castelli, M.: A Copernicus-based
758 evapotranspiration dataset at 100 m spatial resolution over four Mediterranean
759 basins, *Earth Syst. Sci. Data*, 16, 4709-4734. 10.5194/essd-16-4709-2024, 2024.

760 Berbery, E. H., Mitchell, K. E., Benjamin, S., Smirnova, T., Ritchie, H., Hogue, R. and
761 Radeva, E.: Assessment of land - surface energy budgets from regional and
762 global models, *J. Geophys. Res.-Atmos.*, 104, 19329-19348.
763 10.1029/1999jd900128, 1999.

764 Betts, A. K., Ball, J. H., Beljaars, A. C. M., Miller, M. J. and Viterbo, P. A.: The land
765 surface - atmosphere interaction: A review based on observational and global
766 modeling perspectives, *J. Geophys. Res.-Atmos.*, 101, 7209-7225.
767 10.1029/95jd02135, 1996.

768 Castelli, M., Anderson, M. C., Yang, Y., Wohlfahrt, G., Bertoldi, G., Niedrist, G.,
769 Hammerle, A., Zhao, P., Zebisch, M. and Notarnicola, C.: Two-source energy
770 balance modeling of evapotranspiration in Alpine grasslands, *Remote Sens. Environ.*, 209,
771 327-342. 10.1016/j.rse.2018.02.062, 2018.

772 Chen, J., He, T., Jiang, B. and Liang, S.: Estimation of all-sky all-wave daily net
773 radiation at high latitudes from MODIS data, *Remote Sens. Environ.*, 245,
774 111842. 10.1016/j.rse.2020.111842, 2020.

775 de Wit, A. J. W., Boogaard, H. L. and van Diepen, C. A.: Spatial resolution of
776 precipitation and radiation: The effect on regional crop yield forecasts, *Agric. For. Meteorol.*, 135, 156-168. 10.1016/j.agrformet.2005.11.012, 2005.

777 Du, Y., Wang, T., Zhou, Y., Letu, H., Li, D. and Xian, Y.: Towards user-friendly all-sky
778 surface longwave downward radiation from space: General scheme and product,
779 *Bull. Amer. Meteorol. Soc.*, 105, E1303–E1319. 10.1175/bams-d-23-0126.1,
780 2024.

781 ElGhawi, R., Kraft, B., Reimers, C., Reichstein, M., Körner, M., Gentine, P. and
782 Winkler, A. J.: Hybrid modeling of evapotranspiration: inferring stomatal and
783 aerodynamic resistances using combined physics-based and machine learning,
784 *Environ. Res. Lett.*, 18, 034039. 10.1088/1748-9326/acbbe0, 2023.

785 Ersi, C., Sudu, B., Song, Z., Bao, Y., Wei, S., Zhang, J., Tong, Z., Liu, X., Le, W. and
786 Rina, S.: The potential of NIRvP in estimating evapotranspiration, *Remote Sens. Environ.*, 315, 114405. 10.1016/j.rse.2024.114405, 2024.

789 Han, Q., Zeng, Y., Zhang, L., Wang, C., Prikaziuk, E., Niu, Z. and Su, B.: Global long
790 term daily 1 km surface soil moisture dataset with physics informed machine
791 learning, *Sci. Data*, 10, 101. 10.1038/s41597-023-02011-7, 2023.

792 Huang, J., Yu, H., Guan, X., Wang, G. and Guo, R.: Accelerated dryland expansion
793 under climate change, *Nat. Clim. Chang.*, 6, 166-171. 10.1038/nclimate2837,
794 2015.

795 Huang, L., Luo, Y., Chen, J. M., Tang, Q., Steenhuis, T., Cheng, W. and Shi, W.:
796 Satellite-based near-real-time global daily terrestrial evapotranspiration
797 estimates, *Earth Syst. Sci. Data*, 16, 3993-4019. 10.5194/essd-16-3993-2024,
798 2024.

799 Jia, B., Xie, Z., Dai, A., Shi, C. and Chen, F.: Evaluation of satellite and reanalysis
800 products of downward surface solar radiation over East Asia: Spatial and
801 seasonal variations, *J. Geophys. Res.-Atmos.*, 118, 3431-3446.
802 10.1002/jgrd.50353, 2013.

803 Jiang, B., Zhang, Y., Liang, S., Wohlfahrt, G., Arain, A., Cescatti, A., Georgiadis, T., Jia,
804 Kieley, G., Lund, M., Montagnani, L., Magliulo, V., Ortiz, P. S., Oechel, W.,
805 Vaccari, F. P., Yao, Y. and Zhang, X.: Empirical estimation of daytime net
806 radiation from shortwave radiation and ancillary information, *Agric. For.
807 Meteorol.*, 211-212, 23-36. 10.1016/j.agrformet.2015.05.003, 2015.

808 Jiao, B., Su, Y., Li, Q., Manara, V. and Wild, M.: An integrated and homogenized global
809 surface solar radiation dataset and its reconstruction based on a convolutional
810 neural network approach, *Earth Syst. Sci. Data*, 15, 4519-4535. 10.5194/essd-
811 15-4519-2023, 2023.

812 Jung, M., Koirala, S., Weber, U., Ichii, K., Gans, F., Camps-Valls, G., Papale, D.,
813 Schwalm, C., Tramontana, G. and Reichstein, M.: The FLUXCOM ensemble of
814 global land-atmosphere energy fluxes, *Sci. Data*, 6, 74. 10.1038/s41597-019-
815 0076-8, 2019.

816 Kim, Y., Park, H., Kimball, J. S., Colliander, A. and McCabe, M. F.: Global estimates
817 of daily evapotranspiration using SMAP surface and root-zone soil moisture,
818 *Remote Sens. Environ.*, 298, 113803. 10.1016/j.rse.2023.113803, 2023.

819 Li, B., Ryu, Y., Jiang, C., Dechant, B., Liu, J., Yan, Y. and Li, X.: BESSv2.0: A satellite-
820 based and coupled-process model for quantifying long-term global land-
821 atmosphere fluxes, *Remote Sens. Environ.*, 295, 113696.
822 10.1016/j.rse.2023.113696, 2023.

823 Liang, S., Wang, D., He, T. and Yu, Y.: Remote sensing of earth's energy budget:
824 synthesis and review, *Int. J. Digit. Earth*, 12, 737-780.
825 10.1080/17538947.2019.1597189, 2019.

826 Liang, S., Zheng, T., Liu, R., Fang, H., Tsay, S. C. and Running, S.: Estimation of
827 incident photosynthetically active radiation from Moderate Resolution Imaging
828 Spectrometer data, *J. Geophys. Res.-Atmos.*, 111, D15208.
829 10.1029/2005jd006730, 2006.

830 Liu, S., Xu, Z., Song, L., Zhao, Q., Ge, Y., Xu, T., Ma, Y., Zhu, Z., Jia, Z. and Zhang,

831 F.: Upscaling evapotranspiration measurements from multi-site to the satellite
832 pixel scale over heterogeneous land surfaces, *Agric. For. Meteorol.*, 230, 97-113.
833 10.1016/j.agrformet.2016.04.008, 2016.

834 Mohan, M. M. P., Kanchirapuzha, R. and Varma, M. R. R.: Review of approaches for
835 the estimation of sensible heat flux in remote sensing-based evapotranspiration
836 models, *J. Appl. Remote Sens.*, 14, 041501-041501. 10.1111/jrs.14.041501,
837 2020.

838 Mu, Q., Zhao, M. and Running, S. W.: Improvements to a MODIS global terrestrial
839 evapotranspiration algorithm, *Remote Sens. Environ.*, 115, 1781-1800.
840 10.1016/j.rse.2011.02.019, 2011.

841 Mueller, R. W., Matsoukas, C., Gratzki, A., Behr, H. D. and Hollmann, R.: The CM-
842 SAF operational scheme for the satellite based retrieval of solar surface
843 irradiance—A LUT based eigenvector hybrid approach, *Remote Sens. Environ.*,
844 113, 1012-1024. 10.1016/j.rse.2009.01.012, 2009.

845 Muñoz-Sabater, J., Dutra, E., Agustí-Panareda, A., Albergel, C., Arduini, G., Balsamo,
846 G., Boussetta, S., Choulga, M., Harrigan, S., Hersbach, H., Martens, B.,
847 Miralles, D. G., Piles, M., Rodríguez-Fernández, N. J., Zsoter, E., Buontempo,
848 C. and Thépaut, J.-N.: ERA5-Land: a state-of-the-art global reanalysis dataset
849 for land applications, *Earth Syst. Sci. Data*, 13, 4349-4383. 10.5194/essd-13-
850 4349-2021, 2021.

851 Nemani, R. R., Keeling, C. D., Hashimoto, H., Jolly, W. M., Piper, S. C., Tucker, C. J.,
852 Myneni, R. B. and Running, S. W.: Climate-driven increases in global terrestrial
853 net primary production from 1982 to 1999, *Science*, 300, 1560-1563.
854 10.1126/science.1082750, 2003.

855 O., S. and Orth, R.: Global soil moisture data derived through machine learning trained
856 with in-situ measurements, *Sci. Data*, 8, 170. 10.1038/s41597-021-00964-1,
857 2021.

858 Peng, Z., Letu, H., Wang, T., Shi, C., Zhao, C., Tana, G., Zhao, N., Dai, T., Tang, R.,
859 Shang, H., Shi, J. and Chen, L.: Estimation of shortwave solar radiation using
860 the artificial neural network from Himawari-8 satellite imagery over China,
861 *Journal of Quantitative Spectroscopy and Radiative Transfer*, 240, 106672.
862 10.1016/j.jqsrt.2019.106672, 2020.

863 Rios, G. and Ramamurthy, P.: A novel model to estimate sensible heat fluxes in urban
864 areas using satellite-derived data, *Remote Sens. Environ.*, 270, 112880.
865 10.1016/j.rse.2021.112880, 2022.

866 Ryu, Y., Jiang, C., Kobayashi, H. and Detto, M.: MODIS-derived global land products
867 of shortwave radiation and diffuse and total photosynthetically active radiation
868 at 5 km resolution from 2000, *Remote Sens. Environ.*, 204, 812-825.
869 10.1016/j.rse.2017.09.021, 2018.

870 Sellers, P. J., Dickinson, R. E., Randall, D. A., Betts, A. K., Hall, F. G., Berry, J. A.,
871 Collatz, G. J., Denning, A. S., Mooney, H. A., Nobre, C. A., Sato, N., Field, C.
872 B. and Henderson-Sellers, A.: Modeling the Exchanges of Energy, Water, and

873 Carbon Between Continents and the Atmosphere, *Science*, 275, 502-509.
874 10.1126/science.275.5299.502, 1997.

875 Sun, S., Bi, Z., Xiao, J., Liu, Y., Sun, G., Ju, W., Liu, C., Mu, M., Li, J., Zhou, Y., Li,
876 X., Liu, Y. and Chen, H.: A global 5 km monthly potential evapotranspiration
877 dataset (1982–2015) estimated by the Shuttleworth–Wallace model, *Earth Syst.
878 Sci. Data*, 15, 4849-4876. 10.5194/essd-15-4849-2023, 2023.

879 Tang, R., Peng, Z., Liu, M., Li, Z.-L., Jiang, Y., Hu, Y., Huang, L., Wang, Y., Wang, J.,
880 Jia, L., Zheng, C., Zhang, Y., Zhang, K., Yao, Y., Chen, X., Xiong, Y., Zeng, Z.
881 and Fisher, J. B.: Spatial-temporal patterns of land surface evapotranspiration
882 from global products, *Remote Sens. Environ.*, 304, 114066.
883 10.1016/j.rse.2024.114066, 2024a.

884 Tang, R., Wang, J., Liu, M. and Li, Z.-L.: Energy-conservation datasets of global land
885 surface radiation and heat fluxes from 2000-2020 generated by CoSEB,
886 National Tibetan Plateau / Third Pole Environment Data Center. [data set],
887 <https://doi.org/10.11888/Terre.tpdc.302559>, 2025a.

888 Tang, R., Wang, J., Liu, M. and Li, Z.-L.: Energy-conservation datasets of global land
889 surface radiation and heat fluxes from 2000-2020 generated by CoSEB, *Science
890 Data Bank: Science Data Bank*. [data set],
891 <https://doi.org/10.57760/sciencedb.27228>, 2025b.

892 Tang, W., He, J., Qi, J. and Yang, K.: A dense station-based, long-term and high-
893 accuracy dataset of daily surface solar radiation in China, *Earth Syst. Sci. Data*,
894 15, 4537-4551. 10.5194/essd-15-4537-2023, 2023.

895 Tang, W., He, J., Shao, C., Song, J., Yuan, Z. and Yan, B.: Constructing a long-term
896 global dataset of direct and diffuse radiation (10 km, 3 h, 1983–2018) separating
897 from the satellite-based estimates of global radiation, *Remote Sens. Environ.*,
898 311, 114292. 10.1016/j.rse.2024.114292, 2024b.

899 Tang, W., Yang, K., Qin, J., Li, X. and Niu, X.: A 16-year dataset (2000–2015) of high-
900 resolution (3 h, 10 km) global surface solar radiation, *Earth Syst. Sci. Data*, 11,
901 1905-1915. 10.5194/essd-11-1905-2019, 2019.

902 Twine, T. E., Kustas, W. P., Norman, J. M., Cook, D. R., Houser, P. R., Meyers, T. P.,
903 Prueger, J. H., Starks, P. J. and Wesely, M. L.: Correcting eddy-covariance flux
904 underestimates over a grassland, *Agric. For. Meteorol.*, 103, 279-300.
905 10.1016/S0168-1923(00)00123-4, 2000.

906 van der Tol, C.: Validation of remote sensing of bare soil ground heat flux, *Remote Sens.
907 Environ.*, 121, 275-286. 10.1016/j.rse.2012.02.009, 2012.

908 Wang, D., Liang, S., He, T. and Shi, Q.: Estimation of Daily Surface Shortwave Net
909 Radiation From the Combined MODIS Data, *IEEE Trans. Geosci. Remote
910 Sensing*, 53, 5519-5529. 10.1109/tgrs.2015.2424716, 2015.

911 Wang, D., Liang, S., Li, R. and Jia, A.: A synergic study on estimating surface
912 downward shortwave radiation from satellite data, *Remote Sens. Environ.*, 264,
913 112639. 10.1016/j.rse.2021.112639, 2021.

914 Wang, J., Tang, R., Liu, M., Jiang, Y., Huang, L. and Li, Z.-L.: Coordinated estimates

915 of 4-day 500 m global land surface energy balance components, *Remote Sens.*
916 *Environ.*, 326, 114795. 10.1016/j.rse.2025.114795, 2025.

917 Wang, K. C., Dickinson, R. E., Wild, M. and Liang, S.: Atmospheric impacts on climatic
918 variability of surface incident solar radiation, *Atmos. Chem. Phys.*, 12, 9581-
919 9592. 10.5194/acp-12-9581-2012, 2012.

920 Wang, T., Shi, J., Ma, Y., Letu, H. and Li, X.: All-sky longwave downward radiation
921 from satellite measurements: General parameterizations based on LST, column
922 water vapor and cloud top temperature, *ISPRS-J. Photogramm. Remote Sens.*,
923 161, 52-60. 10.1016/j.isprsjprs.2020.01.011, 2020.

924 Wang, Y., Hu, J., Li, R., Song, B. and Hailemariam, M.: Remote sensing of daily
925 evapotranspiration and gross primary productivity of four forest ecosystems in
926 East Asia using satellite multi-channel passive microwave measurements, *Agric.
927 For. Meteorol.*, 339, 109595. 10.1016/j.agrformet.2023.109595, 2023.

928 Wild, M.: Global dimming and brightening: A review, *J. Geophys. Res.-Atmos.*, 114,
929 D00D16. 10.1029/2008jd011470, 2009.

930 Wild, M., Folini, D., Schär, C., Loeb, N., Dutton, E. G. and König-Langlo, G.: The
931 global energy balance from a surface perspective, *Clim. Dyn.*, 40, 3107-3134.
932 10.1007/s00382-012-1569-8, 2012.

933 Wild, M. and Liepert, B.: The Earth radiation balance as driver of the global
934 hydrological cycle, *Environ. Res. Lett.*, 0, 025203. 10.1088/1748-
935 9326/5/2/025003, 2010.

936 Xia, X. A., Wang, P. C., Chen, H. B. and Liang, F.: Analysis of downwelling surface
937 solar radiation in China from National Centers for Environmental Prediction
938 reanalysis, satellite estimates, and surface observations, *J. Geophys. Res.-
939 Atmos.*, 111, D09103. 10.1029/2005jd006405, 2006.

940 Xian, Y., Wang, T., Leng, W., Letu, H., Shi, J., Wang, G., Yan, X. and Yuan, H.: Can
941 Topographic Effects on Solar Radiation Be Ignored: Evidence From the Tibetan
942 Plateau, *Geophys. Res. Lett.*, 51, e2024GL108653. 10.1029/2024gl108653,
943 2024.

944 Xu, J., Liang, S. and Jiang, B.: A global long-term (1981–2019) daily land surface
945 radiation budget product from AVHRR satellite data using a residual
946 convolutional neural network, *Earth Syst. Sci. Data*, 14, 2315-2341.
947 10.5194/essd-14-2315-2022, 2022a.

948 Xu, J., Liang, S., Ma, H. and He, T.: Generating 5 km resolution 1981–2018 daily global
949 land surface longwave radiation products from AVHRR shortwave and
950 longwave observations using densely connected convolutional neural networks,
951 *Remote Sens. Environ.*, 280, 113223. 10.1016/j.rse.2022.113223, 2022b.

952 Yao, Y., Liang, S., Li, X., Chen, J., Liu, S., Jia, K., Zhang, X., Xiao, Z., Fisher, J. B.,
953 Mu, Q., Pan, M., Liu, M., Cheng, J., Jiang, B., Xie, X., Grünwald, T., Bernhofer,
954 C. and Roupsard, O.: Improving global terrestrial evapotranspiration estimation
955 using support vector machine by integrating three process-based algorithms,
956 *Agric. For. Meteorol.*, 242, 55-74. 10.1016/j.agrformet.2017.04.011, 2017.

957 Yu, L., Qiu, G. Y., Yan, C., Zhao, W., Zou, Z., Ding, J., Qin, L. and Xiong, Y.: A global
958 terrestrial evapotranspiration product based on the three-temperature model
959 with fewer input parameters and no calibration requirement, *Earth Syst. Sci.*
960 *Data*, 14, 3673-3693. 10.5194/essd-14-3673-2022, 2022.

961 Zhang, C., Long, D., Zhang, Y., Anderson, M. C., Kustas, W. P. and Yang, Y.: A decadal
962 (2008–2017) daily evapotranspiration data set of 1 km spatial resolution and
963 spatial completeness across the North China Plain using TSEB and data fusion,
964 *Remote Sens. Environ.*, 262, 112519. 10.1016/j.rse.2021.112519, 2021.

965 Zhang, J., Zhao, L., Deng, S., Xu, W. and Zhang, Y.: A critical review of the models
966 used to estimate solar radiation, *Renew. Sust. Energ. Rev.*, 70, 314-329.
967 10.1016/j.rser.2016.11.124, 2017.

968 Zhang, K., Kimball, J. S., Nemani, R. R. and Running, S. W.: A continuous satellite -
969 derived global record of land surface evapotranspiration from 1983 to 2006,
970 *Water Resour. Res.*, 46, W09522. 10.1029/2009wr008800, 2010.

971 Zhang, X., Liang, S., Zhou, G., Wu, H. and Zhao, X.: Generating Global LAnd Surface
972 Satellite incident shortwave radiation and photosynthetically active radiation
973 products from multiple satellite data, *Remote Sens. Environ.*, 152, 318-332.
974 10.1016/j.rse.2014.07.003, 2014.

975 Zhang, Y., Kong, D., Gan, R., Chiew, F. H. S., McVicar, T. R., Zhang, Q. and Yang, Y.:
976 Coupled estimation of 500 m and 8-day resolution global evapotranspiration
977 and gross primary production in 2002–2017, *Remote Sens. Environ.*, 222, 165-
978 182. 10.1016/j.rse.2018.12.031, 2019.

979 Zheng, C., Jia, L. and Hu, G.: Global land surface evapotranspiration monitoring by
980 ETMonitor model driven by multi-source satellite earth observations, *J. Hydrol.*,
981 613, 128444. 10.1016/j.jhydrol.2022.128444, 2022.

982